Smoothing sodium metal anode with a self-regulating alloy interface for high-energy and sustainable sodium metal battery

*Lei Wang, Jian Shang, Qiyao Huang, Hong Hu, Yuqi Zhang, Chuan Xie, Yufeng Luo, Yuan Gao, Huixin Wang, Zijian Zheng**

Dr. L. Wang, Dr. J. Shang, Prof. Q. Huang, Dr. H. Hu, Dr. Y. Zhang, X. Chuan, Dr. Y. Luo, Dr. Y. Gao, H. Wang, Prof. Z. Zheng
Laboratory for Advanced Interfacial Materials and Devices, Research Centre for Smart Wearable Technology, Institute of Textiles and Clothing, The Hong Kong Polytechnic University, Hong Kong SAR, China
E-mail: tczzheng@polyu.edu.hk

Prof. Z. Zheng
Research Institute for Smart Energy, The Hong Kong Polytechnic University, Hong Kong SAR, China

Keywords: sodium battery, sodium metal anode, grid storage, interface, energy density

Because of the large abundance of sodium (Na) source and the easy fabrication of Na-containing compounds, sodium (Na) battery is a more environmentally friendly and sustainable technology than lithium-ion battery (LIB). In particular, Na metal batteries (SMBs) are considered promising to realize a high energy density to overtake the cost effectiveness of LIBs, which is critically important in large-scale applications such as grid storage systems. However, the cycling stability of Na metal anode faces significant challenges particularly under high cycling capacities, due to the complex failure models caused by the formation of Na dendrites. Here, we report an universal surface strategy, based on a self-regulating alloy interface of the current collector, to effectively inhibit the formation of Na dendrites. High capacity (10 mAh cm^{-2}) Na metal anode can achieve stable cycling for over 1,000 h with a low overpotential of 35 mV. When paired with high-capacity $Na_3V_2(PO_4)_2F_3$ cathode (7 mAh cm^{-2}), the SMB delivers an unprecedented energy density (calculated based on all the cell components) over 200 Wh kg^{-1} with flooded electrolyte, or over 230 Wh kg^{-1} with lean electrolyte. The dendrite-

free SMB also shows high cycling stability with a capacity retention per cycle over 99.9% and an ultrahigh energy efficiency of 95.8%.

1. Introduction

Grid energy storage is a critical and indispensable component for the utilization of clean and sustainable energy[1-3], the realization of smart city, and the insurance of resilient and reliable electricity to the industry[4]. In comparison to conventional grid storage technologies, including pumped hydro, thermal storage, and compressed air, rechargeable batteries show significant advantages in the conversion efficiency, energy density, and power management[2]. In addition, batteries are easier to deploy for a wide variety of distributed and centralized applications. It is expected that the demand of battery-based grid storage system will reach 4,500 GWh in 2050 [5].

Lithium-ion batteries (LIBs) are the most widely deployed battery technology in grid energy storage nowadays. Although LIBs fulfill the requirement of energy density for grid storage, i.e., 140~200 Wh kg^{-1} [6], the high cost of lithium, which is one of the rare elements, prohibits their large-scale application[7]. Moreover, the purification of Li salt in the industrial manufacture consumes massive energy and toxic chemicals. The mining process of many Li resources will unavoidably sacrifice the environmental benefits, which significantly hinders the sustainable use of Li[8].

In comparison, sodium (Na) batteries are considered as more cost-effective and sustainable options for grid energy storage[9-10] due to the high abundance and accessibility of sodium[11-12]. The battery-grade sodium-containing compounds can be easily produced from the sea water without the need for complex purification processes[13]. The production of the cathodic and anodic materials of Na batteries is much more environmentally friendly when compared with that of LIBs.

The cost-effectiveness of Na batteries are expected to overtake that of LIBs when the practical energy density is above 200 Wh kg^{-1} [14].To achieve this goal, it is critical to develop stable and high-capacitive Na anodes[14]. Anodes based on Na-ion chemistry, including conversion type (metal oxide[15], metal sulfide[16-17]), insertion type (modified graphite[18], hard carbon[19], $Na_2Ti_3O_7$[20]), and alloy type (phosphate[21], tin[22], antimony[23]) have been studied the most in the past decades. However, the energy densities of those state-of-the-art prototypes of Na-ion batteries (SIBs) reported to date are still well below the desirable target, only reaching ~130 Wh kg^{-1} [14, 24-26].

In recent years, Na metal is proposed as anode to build high-energy-density sodium metal batteries (SMBs) owing to the highest capacity (1166 mAh g^{-1}) and lowest redox potential (-2.71 V vs. SHE) of Na[27]. Nevertheless, the cycling performance of SMBs is seriously limited by the uncontrolled growth of Na dendrites [24, 27], as a result of the uneven heterogeneous deposition of Na during the discharge process[28-29]. Despite the development of several approaches to suppressing Na dendrites, which include employing new electrolyte chemistry[30-32], building artificial solid-electrolyte interface (SEI)[33], and designing sodiophilic three-dimensional (3D) host materials[34-35], SMBs nowadays still require a large excess of Na metal with an N/P ratio (area capacity ratio of negative to positive electrodes) much higher than 10 (Table S1) [36-40]. As a consequence, the reported energy density of SMBs is limited to 60 Wh kg^{-1} (Table S1), even much lower than that of the prototype SIBs mentioned above[25]. For a practical SMB, the Na metal anode should support stable cycling at a high capacity with a controlled N/P ratio[41]. Up to now, it remains a significant challenge to realize a stable SMB with practical areal capacity.

Herein, we report a self-regulating alloy interface, nickel antimony (NiSb), which enables the smooth deposition of Na metal during the discharge process. A thin layer of NiSb chemically deposited on the current collector regulates the uniform electrochemical plating of Na metal via a reactive formation of protruded Na metal nanoislands and a subsequent lateral

connection and planarization of these islands with additional Na metal, which is different from the conventional "nuclei formation and growth" model of Na deposition on the sodiaphilic substrate[42-44]. We demonstrate that this self-regulating mechanism enabled by the alloy interface effectively lowers the overpotential and offers dendrite-free plating/stripping of Na metal over 1,000 h at an exceedingly high areal capacity of 10 mAh cm^{-2}. We further pair the stable Na metal anodes with thick cathodes made of sodium vanadium fluoride phosphate (NVPF). The full cell delivers an ultrahigh areal capacity of ~7 mAh cm^{-2} and reaches a remarkable energy density over 200 Wh kg^{-1} with taking the total weight of the current collectors, electrodes, separator, and flooded electrolyte into account. Profiting from this unique feature of the smoothing deposition, the full cell could stably cycle over 230 cycles with a high capacity retention of 99.92% per cycle and ultrahigh energy efficiency of 95.8%. We further demonstrate that the energy density can overpass 230 Wh kg^{-1} when using lean electrolyte. More importantly, we demonstrate that this self-regulating mechanism is an universal strategy to protect other alkali metal anodes such as Li and K.

2. Results and Discussion

2.1. Self-regulating mechanism of NiSb

As shown in **Figure 1**a, the self-regulating mechanism lies on the electrochemical reaction between Na^+ ions and NiSb interface during plating, to form chemically sodiophilic yet electron-hindered semiconducting Na_3Sb nano-islands and the sodiophobic yet electron-favored conductive Ni matrix.

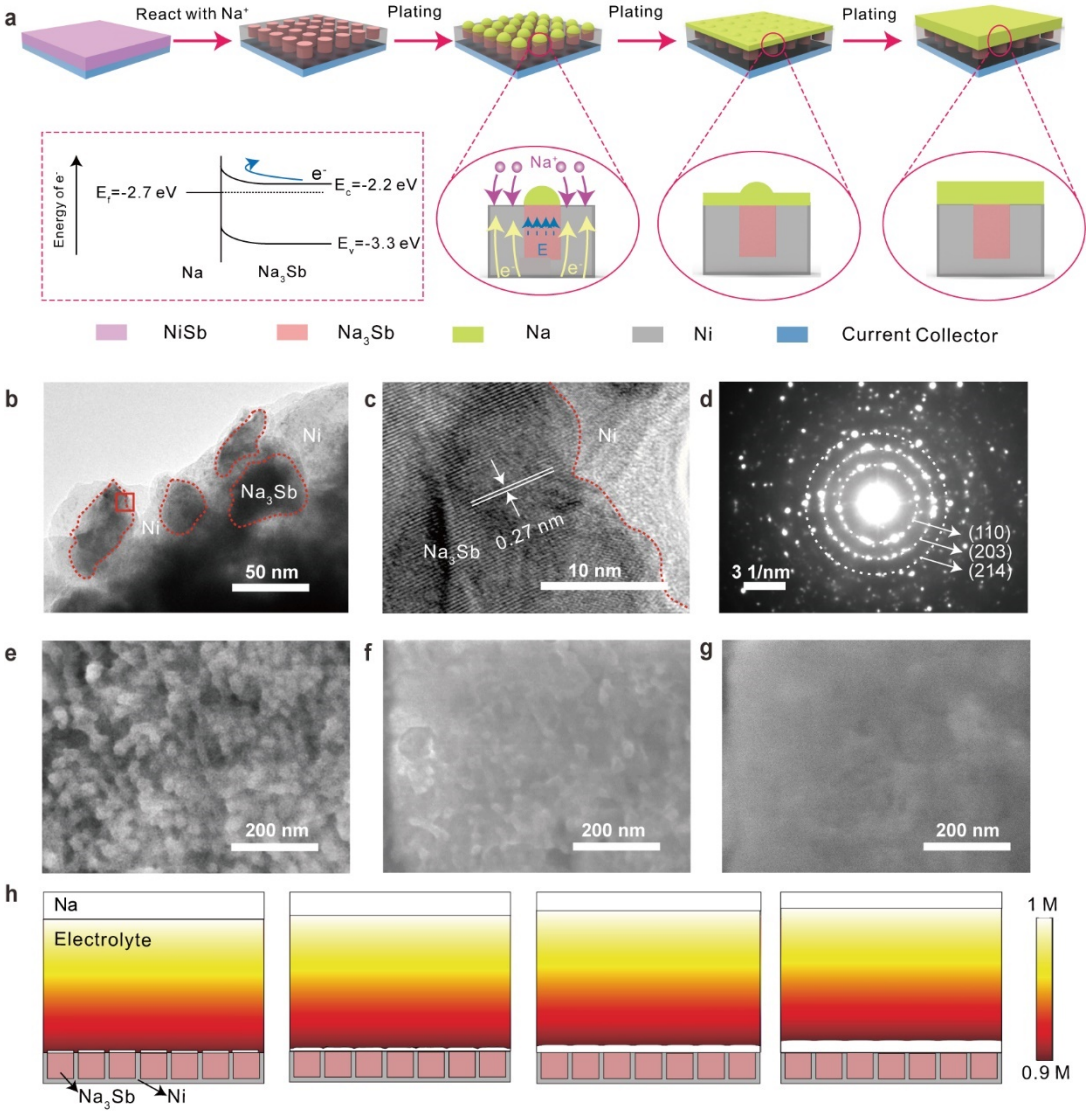

Figure 1. Self-regulating mechanism of Na metal using the alloy interface. a) Schematic illustration of the smoothing deposition by the self-regulating mechanism. NiSb firstly reacts with Na ions to form the Na_3Sb/Ni heterostructure. Na favorably nucleates on the Na3Sb due to the sodiophilicity. The energy barriers built at the interface of Na/Na_3Sb block transportation of the electrons from the Na_3Sb to Na seeds and thus hinder the growth of Na seeds. The following deposition connects Na seeds and further enables a smooth film of Na. b) Transmission electron microscope (TEM) image with low magnification for the sodiated NiSb at 0.01 V. The areas within the red dot line correspond to Na_3Sb, confirming the size of Na_3Sb nano islands is between 30-50 nm. c) High-resolution TEM image of the area in the red box in b. d) The selected areal electron diffraction (SAED) pattern of the sodiated NiSb. The circled spots in the pattern correspond to the Na_3Sb. The diffuse ring near the transmission spots proves the amorphous materials, which could be ascribed to the amorphous Ni matrix around the Na_3Sb after the complete sodiation of NiSb. e) Scanning electron microscope (SEM) image for the deposited Na at the capacity of 0.05 mAh cm^{-2}. The uniform Na seeds with the size of ~30 nm can be observed. f) SEM image of the deposited Na at the capacity of 0.1 mAh cm^{-2}. The size of the Na seeds does not become larger and the gaps between the Na seeds are partially filled. g) SEM image of the deposited Na at the capacity of 0.5 mAh cm^{-2}. h) COMSOL simulation of the self-regulating deposition process on the alloy interface. The pink, grey, white areas represent the Na3Sb nano islands, amorphous Ni matrix, and Na, respectively. Gradient color

in electrolyte corresponds to the local concentration of Na ions. The M in the figure represents the molarity.

As a proof of concept, a thin and uniform layer of NiSb was deposited on the upper surface of the current collector made of metal foil by a galvanic displacement reaction (see Experimetal Section/Methods for the detailed description of the experiment). The NiSb-coated current collector showed a smooth topography (Figure S1). Na metal was then electrochemically plated onto the NiSb-coated substrate by discharging to 0 V. Due to the excellent conductivity of the current collector, the whole electrode shared with same voltage, which could gurantee the even sodiation of NiSb. During the initial stage of the electrochemical deposition, Na^+ ions first reacted with NiSb completely according to equation (1)[45-47], which formed uniform structure where islands of Na_3Sb embedded in the Ni matrix (Figure 1b and Figure S2) at the interface. The size of the Na_3Sb islands was ca. 20~40 nm (transmission electronic microscopy, TEM, Figure 1c), and the Ni matrix was amorphous according to the measurement with selected areal electron diffraction (SAED, Figure 1d).

$$NiSb + 3Na^+ + 3e^- \rightarrow Na_3Sb + Ni \quad (1)$$

In the subsequent plating process, Na metal was preferably deposited on the surface of the Na_3Sb islands due to the higher affinity of Na to Na_3Sb than to Ni. These Na metal seeds showed a typical size of ~30 nm, which matched well with the size of the underlying Na_3Sb islands (Figure 1e). The heterojunction of Na/Na_3Sb created a built-in electric barrier blocking the electron transport from Na_3Sb to Na[48], which prevented the further growth of the Na metal seeds (Figure 1f and Figure S3). At this point, Na would deposit on the surrounding Ni surface, which eventually connected the isolated Na metal seeds and smoothened the whole surface of the deposited Na metal anode (Figure 1g). In comparison, depositing Na metal on the pristine or Sb-coated current collector resulted in conventional heterogeneous nucleation and growth of Na metal, such that the surfaces of as-deposited Na metal became very rough and were rich in dendritic Na or mossy pores (Figure S4).

We simulated the deposition of Na metal on the unmodified and NiSb-coated current collector using COMSOL Multiphysics (see Experimetal Section/Methods for detailed parameters of the simulation). For the NiSb-coated substrate, small Na_3Sb domains were separated by Ni matrix in the simulation. It can be seen from the simulation results that one Na nuclei appeared on each Na_3Sb domain at the initial stage, and then Na metal deposited on the Ni domains, which eventually formed a flat Na metal film (Figure 1h). In sharp contrast, a Na apex first appeared on the pristine current collector and then immediately grew to a large needle (Figure S5). These simulation results are in good agreements with the experimental observations.

Such a unique self-regulating mechanism enables the effective suppression of dendrite growth. As a proof-of-concept demonstration, we recorded the *in situ* morphological evolution of Na metal plated on the pristine current collector, NiSb-modified current collector, and a graphite film by operando optical microscopy (Figure S6). For plating occurring on the pristine current collector and graphite film, small protrusions of Na dendrites started to grow on the upper surface (counter to the Na metal source) of the substrates at the initial plating stage (**Figure 2**a and 2b, Movie S1 and S2). After plating for 2 min, the overflowed Na dendrites appeared at the sides of the substrates. As soon as the dendritic Na covered the entire surface of the substrates, the incrassation of the highly porous Na dendrites was accelerated. In contrast, the surface of NiSb-modified current collector remained smooth and no dendrite was observed during the whole electrochemical deposition (Figure 2c and Movie S3).

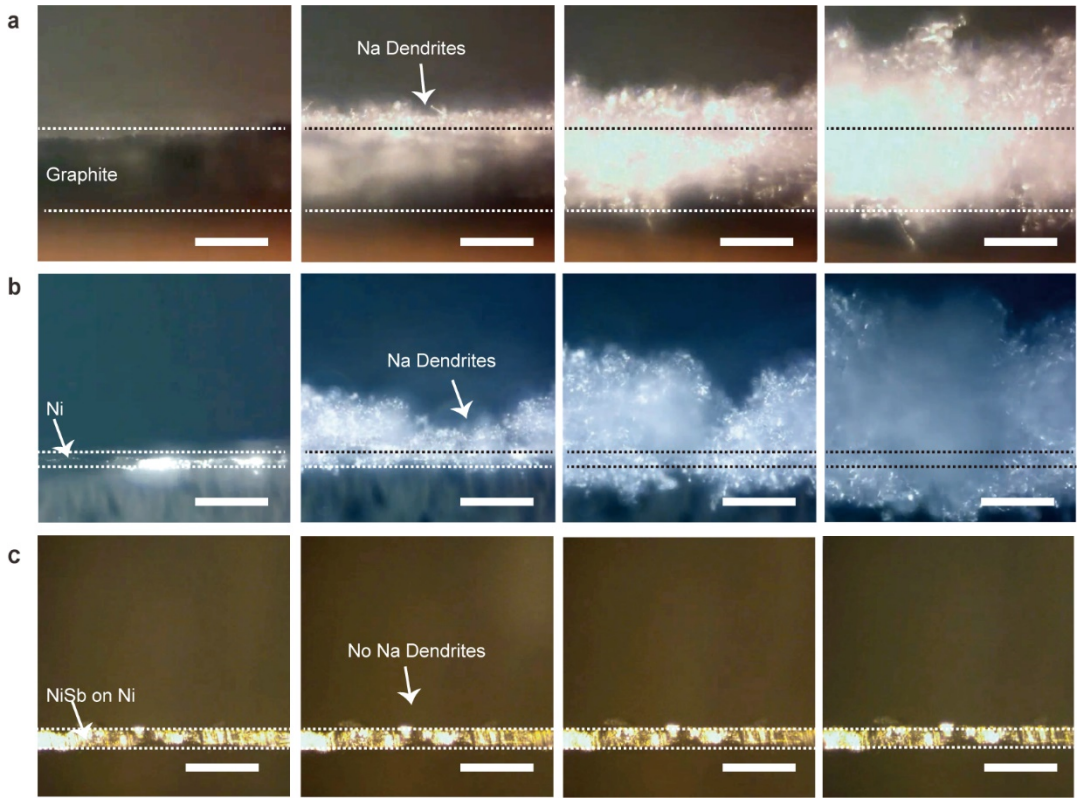

Figure 2. Inhibition of the growth of Na dendrites on the intermetallic interface. Operando observation of the Na plating on a) a graphite film; b) a Ni foil and c) a NiSb-coated current collector. A large number of Na dendrites can be observed on the surfaces of the graphite and Ni foil, while no Na dendrite is observed on the NiSb-coated current collector. The black or white dot lines in the figures are the reference lines for the pristine current collectors. (scale bars of all images: 100 μm)

2.2. Dendrite-free and stable cycling of high-areal-capacity Na metal anodes

To test the stability of high-areal-capacity Na metal anodes, we used NiSb-coated carbon cloth (NiSb-CC) as the current collector, which ensured a large interfacial area between the Na metal and the NiSb. Carbon cloth (CC) owned a large electrochemically effective area (43 folds higher than a foil of the same projective size, Figure S7 and Supporting text 1), excellent mechanical flexibility and stability. As illustrated in **Figure 3**a, we deposited a uniform layer of Ni on the CC (Figure 3b) via a polymer-assisted metal deposition method (PAMD)[49] to obtain the Ni-coated CC (Ni-CC). The thin Ni layer was uniformly coated on the surface of each carbon fiber and the sheet resistance of Ni-CC was 0.48 Ω cm^{-2} (Figure 3c and Figure S8). We then transformed the Ni-CC into the NiSb-CC by the galvanic displacement described above. The NiSb coating was also conformably deposited on the carbon surface (Figure 3d) and

the sheet resistance was not altered. X-ray diffraction (XRD), X-ray photoelectron spectroscopy (XPS), and ferromagnetic tests confirmed the total conversion of Ni into NiSb (Figure S9).

We tested the Coulombic efficiency (CE) of the Na metal anode by repeatedly depositing and fully stripping Na metal onto different current collectors at a practical capacity of 3.5 mAh cm^{-2}. The Na metal anode deposited on NiSb-CC exhibit the highest average CE of 99.74% and the most extended cycling life (Figure 3e). The galvanostatic discharge-charge (GCD, Figure 3f) profiles of the anode over the first 100 cycles well overlapped, indicating the excellent reversibility of the Na metal on NiSb-CC. After cycling, the Na metal pertained smooth morphology without any sign of Na dendrite or dead Na or thick SEI (Figure 3g).

We also monitored the plating of Na metal on NiSb-CC with increased capacities to 6, 10, and 20 mAh cm^{-2}. Importantly, Na metal only deposited densely and smoothly on the NiSb surfaces on the fibers and occupied the internal space of the yarns during the entire plating process, and the gaps between the yarns remained largely unfilled (Figure S10), which also indicated the remarkable affinity of Na to NiSb. In obvious contrast, the CEs of Na metal anodes deposited on CC, Sb-CC, and Ni-CC were only 96.02% (first 50 cycles), 98.20% (first 50 cycles), and 87.03% (first 12 cycles), respectively. After that, the CEs rapidly dropped below 80%. The phenomenon of low CEs was attributed to the formation of a large amount of mossy or needle-like dead Na and thick solid-electrolyte interface (SEI) layers (Figure S11). The surface of Na metal became even rougher with increased plated capacities, and large blocks of Na metal of tens to hundreds of micrometers were observed randomly on the surface of unmodified CC (Figure S12). We also prepared the amorphous Ni coated CC (aNi-CC, Figures S13 a and b) and lots of Na beads or dendrites could be observed on the fibers of both the Ni-CC (Figure S13c) and aNi-CC (Figure S13d).

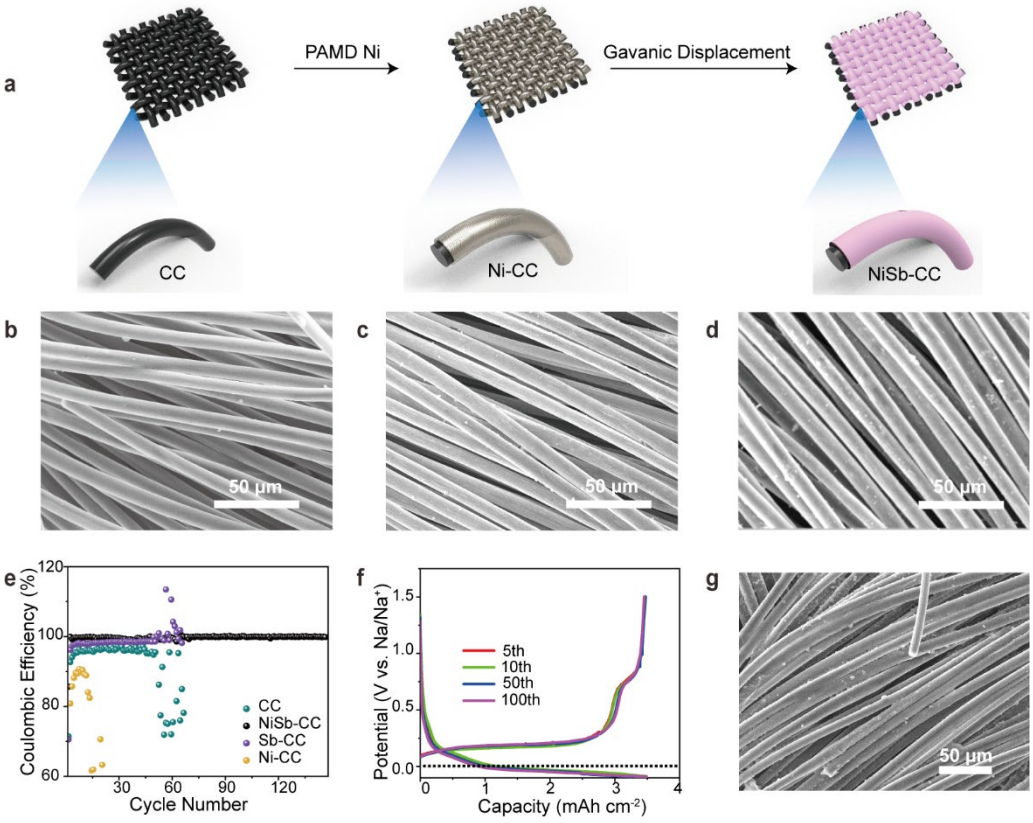

Figure 3. High-areal-capacity Na metal anode on NiSb-coated carbon cloth (NiSb-CC). a) Fabrication procedure of NiSb-CC. b-d) SEM images for the pristine carbon cloth (CC), Ni-coated CC (Ni-CC), and NiSb-CC. e) Comparison of the Coulombic efficiency (CE) of the full stripping and deposition of Na metal on different CC-based current collectors at a capacity of 3.5 mAh cm^{-2}. f) Galvanostatic discharge-charge (GCD) profiles of the striping and plating of Na on different current collectors. g) Post-mortem SEM image of the NiSb-CC after 53 full deposition-and-stripping cycles. No dead Na or Na dendrite is observed.

2.3. High-speed fabrication of stable Na metal anodes with molten Na

Electrodeposition is a time-consuming method to fabricate Na metal anodes in practical applications. Here, we demonstrate the rapid fabrication of high-capacitive and stable Na metal anodes by direct wicking of the molten Na into the NiSb-CC (**Figure 4**a). We first melted the Na metal and then placed the NiSb-CC at the edge of the molten Na, which could be rapidly infused into the NiSb-CC due to the high affinity of NiSb to Na. After cooling down, we obtained a composite-like Na metal anode (Na-NiSb-CC). As a result of the sodiophilicity of NiSb (Figure S14), Na metal smoothly wrapped each fiber but did not fill the gaps between the yarns (Figure 4b, 4c, and Figure S15a). The mass loading of Na metal was ~18 mg cm^{-2},

corresponding to an areal capacity of ~21 mAh cm^{-2}. The entire fabrication took ~30 seconds (Movie S4). In comparison, molten Na could not wet CC or Ni-CC. Soaking CC and Ni-CC in the molten Na for more than 6 minutes (Movie S5 and S6) resulted in the non-uniformed coating of Na metal to obtain the CC and Ni-CC based Na composite (Na-CC and Na-Ni-CC, Figure S15b-e).

As shown in Figure 4e, the GCD test of Na-NiSb-CC displayed a low overpotential of 35.0 mV and a flat and stable voltage profile, indicating a sodiophilic and dendrite-free behavior during the plating and stripping of Na metal. In contrast, the overpotentials were much larger for Na-CC (46.2 mV), Na-Ni-CC (39.6 mV), aNi-CC based Na composite (50 mV, Figure S16) and Na plate (54.8 mV). Moreover, obvious fluctuation of the GCD profiles occurred, which is evidence of the formation of Na dendrites [50].

The Na-NiSb-CC possessed a stable GCD profile over 2,000 h of charge/discharge cycles of 1 mAh cm^{-2} at a current density of 1 mA cm^{-2}. Under the same testing conditions, the Na plate, Na-CC, Na-Ni-CC and Na-aNi-CC failed after 45 h, 158 h, 121 h and 104 h (Figure S16), respectively (Figure 4f). When the cycling capacity was increased to 10 mAh cm^{-2}, which was equivalent to a high depth of deposition (DOD) over 47%, the Na-NiSb-CC could also display a stable cycling for over 1,000 h (Figure 4g). When the current density was increased to 5 mA cm^{-2}, Na-NiSb-CC pertained a flat and stable GCD profile during the cycling, while the control samples showed sharply increased overpotentials (Figure 4h).

To understand the SEI evolution of the Na-NiSb-CC, we stripped a small amount of Na from the composite. Na near the separator was totally stripped and the alloy interface was exposed (Figure S17). In the following deposition process, this exposed alloy interface could still play the self-regulating function and the unstripped Na at the bottom would compensate the Na loss during the following cycling process. The cycled Na redistributed on fibers of sodiated NiSb-CC and showed a smooth surface after 50th cycling (Figure S18a). The elemental distribution of F, which came from the NaF in the SEI, was uniform on the surface

of Na (Figure S18b). The unstripped part of the Na metal still protected the fibers. From the cross-sectional images, no F could be observed in the unstripped Na. According to the above results, the SEI evolution could be concluded as follows (Figure S18c). First of all, at the initial state, the SEI forms on the upper surface of the Na on the fibers. During the full encapsulation of Na on the fibers, no SEI could be formed on the fibers. After few cycles, the Na near the upper surface of the yarns was stripped and deposited back to the surface of the fibers because of the self-regulating interface, and the SEI covered on the Na. At the final state, the redistribution of the Na ended and SEI covered on the Na surface of every fiber inside the yarns.

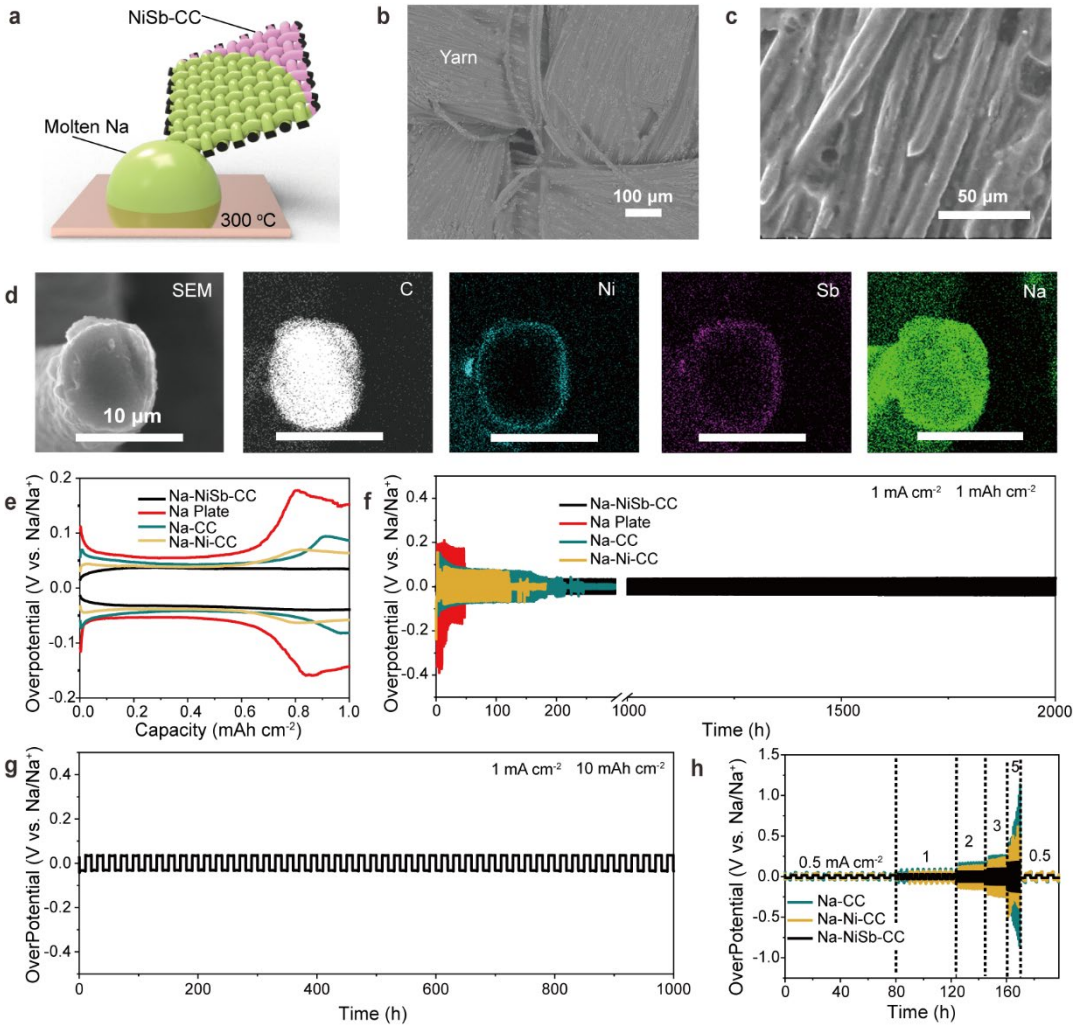

Figure 4. Fast fabrication of high-areal-capacity Na metal anode. a) Schematic illustration of the fabrication of the high-areal-capacity Na metal anode on NiSb-CC (Na-NiSb-CC) via a melt infusion process. b) Low-magnification SEM image of the Na-NiSb-CC. Na is confined in the yarn of the Na-NiSb-CC fabrics. c) High-resolution SEM image of the Na-NiSb-CC. Na wraps

every fiber in the NiSb-CC. d) SEM and elemental mapping of the single fiber of the Na-NiSb-CC. The alloy coating layer remains intact during the thermal infusion process and Na coating is uniform on the fiber. e) GCD profiles of the symmetrical cells composed of different Na anodes. f) Comparison of the durability of symmetrical cells with Na metal anodes based on different hosts at 1 mAh cm^{-2}. g) Cycling stability of the symmetrical cell composed of Na-NiSb-CC at the areal capacity of 10 mAh cm^{-2}. h) Comparison of the rate capability of symmetrical cells based on different sodium metal anodes at current densities from 0.5 mA cm^{-2} to 5 mA cm^{-2}. The cycling capacity is 1mAh cm^{-2}.

2.4. Stable SMBs with practical energy density over 200 Wh kg^{-1}

The low overpotential and high stability of the Na-NiSb-CC at high DOD offer a significant advantage in constructing high-energy-density SMBs. As a proof of concept, we pair the Na-NiSb-CC anode with NVPF cathode (**Figure 5**a) because of the high specific energy (507 Wh kg^{-1}), high ionic conductivity, excellent reversibility, and rate capability of NVPF[51-52].

Binder-free NVPF cathodes with different capacities, noted as NVPF-Ni-CF, were fabricated on Ni-coated carbon felts via an *in-situ* synthesis method (see Figure S19 and Experimetal Section/Methods for the detailed description of the fabrication process). At an areal capacity of 1.49 mAh cm^{-2}, the battery with Na-NiSb-CC anode (NVPF-Ni-CF||Na-NiSb-CC) showed a high initial CE of 95%, which was resulted from the irreversible side reaction between the Na metal and the carbonate electrolyte. The SEI formed in this process possessed a quite stable conponents during cycling (Figure S20). The cell displayed outstanding cycle stability with a high-capacity retention per cycle of 99.96% over 1,000 cycles (Figure 5b and Figure S21a). In comparison, the capacity of the full cell using the same NVPF cathode but paired with Na-CC (NVPF-Ni-CF||Na-CC) dropped rapidly to almost zero after 60 cycles. These results demonstrate that the self-regulating feature of the NiSb is indispensable for long-term cycling of the full cells.

In order to achieve a high energy density over 200 Wh kg^{-1} at the cell level, a benchmark value determining the commercial competitiveness of Na batteries for grid storage[6], the areal

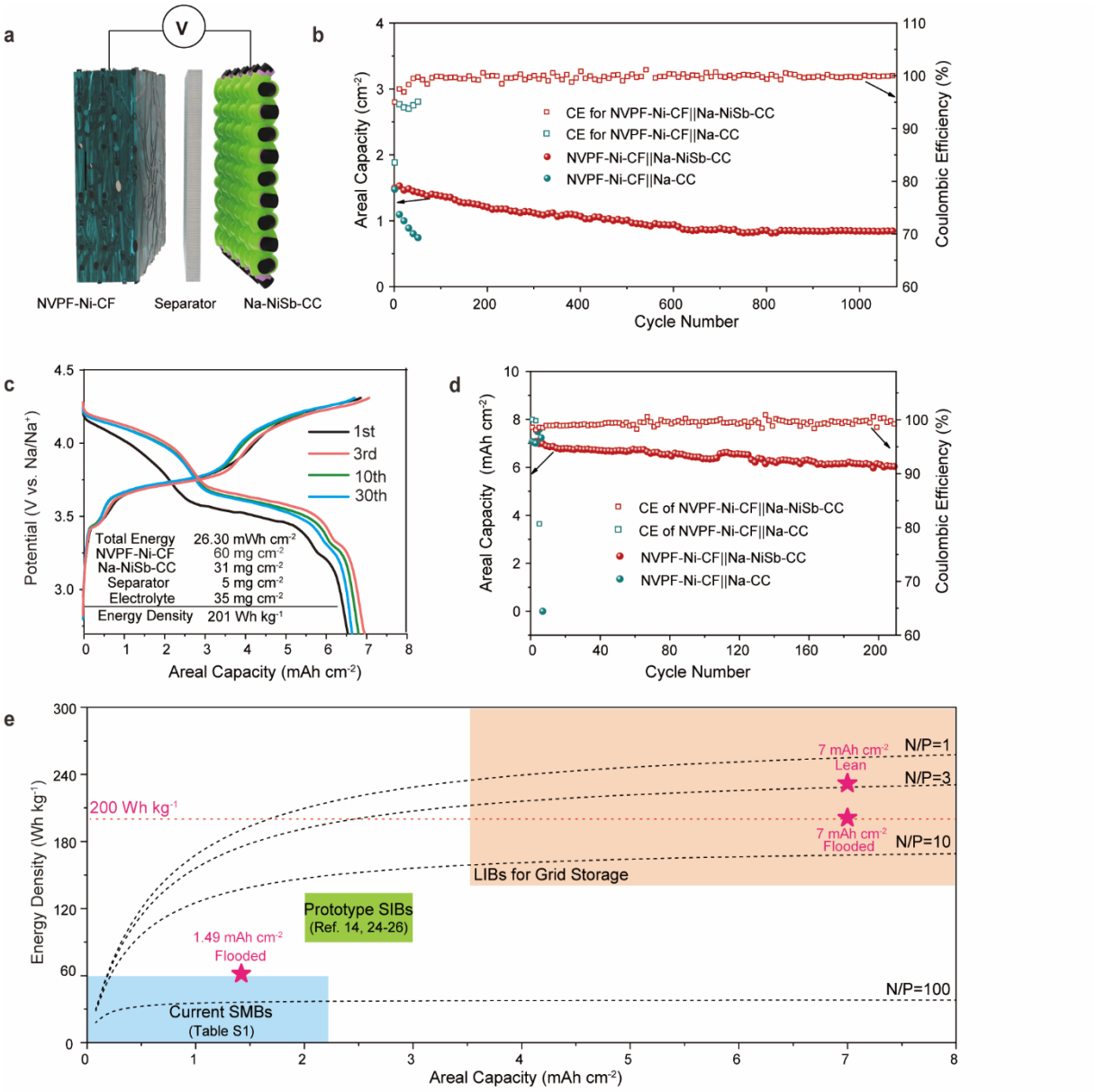

Figure 5. Electrochemical performance of high-energy-density sodium metal battery. a) A scheme of the structure of the full cell of NVPF-Ni-CF||Na-NiSb-CC. b) Comparison of the cycling stability of the NVPF-Ni-CF||Na-NiSb-CC and NVPF-Ni-CF||Na-CC cells. The cathode is made by growing NVFP on Ni-coated carbon felt (NVPF-Ni-CF). The mass loading of NVPF is 11.6 mg cm^{-2}. c) GCD profiles of the NVPF-Ni-CF||Na-NiSb-CC cell with a high capacitive cathode at different cycles. The total energy of the cell is calculated based on the GCD profile of the 3rd cycle. d) Cycling stability of the full cells based on Na-NiSb-CC cathode cycled at an areal capacity of 7 mAh cm^{-2} with 200% oversized Na. e) Comparison of the energy density of this work with those of reported Na based batteries. The black dot lines are the reference lines for the energy density of conventional NVPF||Na. The calculation method refers to Supporting text 2. The red dot line is the reference line of 200 Wh kg^{-1}. The area for the current reported SMBs is sketched according to the data in Table S1.

capacity of the cathode should be well above 3 mAh cm^{-2} and the N/P ratio should be strictly restricted. As a proof of concept, we fabricated a high-capacity NVPF cathode (~7 mAh cm^{-2}) and then paired it with the Na-NiSb-CC anode (~21 mAh cm^{-2}) in the flooded electrolyte to study electrochemical properties, which gave a low N/P ratio of 3. The energy density of the cell calculated based on the GCD profiles and the total weight of the cell components including the current collectors, electrodes, separator, and flooded electrolyte, was 201 Wh kg^{-1} (Figure 5c). After 230 charge/discharge cycles, the cell pertained an areal capacity of ~6 mAh cm^{-2}, which is equivalent to a high capacity retention per cycle of 99.93% (Figure 5d). In comparison, the NVPF-Ni-CF||Na-CC cell acquiring the same areal capacity failed after 3 cycles (Figure S21b). To further improve the energy density and test its potential in real applications, we tested the cell under the lean electrolyte condition (3 mg mAh^{-1}) with a lighter separator membrane. The cell could run well for more than 50 cycles and the energy density was 232 Wh kg^{-1} (Figure S21c and S21d), which showed 15% improvement in energy density compared with the flooded cell.

The energy efficiency, the ratio of the energies involved in the discharge and charge processes, is a critical parameter to evaluate the energy loss in the grid storage system[53]. According to the GCD profile, the energy efficiency was 95.8%, which is much higher than that of many lithium-based energy storage systems[53]. This high energy efficiency can be attributed to the low overpotential of the Na-NiSb-CC anode.

Figure 5e compares the energy density of NVPF-Ni-CF||Na-NiSb-CC with those of state-of-the-art SMBs and prototype SIBs reported in the literature. At an areal capacity of ~7 mAh cm^{-2} and a low N/P ratio of ~3, the energy densities of NVPF-Ni-CF||Na-NiSb-CC cells with flooded or lean electrolyte far exceed the energy densities of the reported SMBs and prototype SIBs and can fulfill the requirements of grid storage. The dash lines in the figure estimate the calculated energy density of a conventional SMB consisting of NVPF, Na plate, and Al foils under the lean electrolyte condition (Supporting text 2) as a function of the areal capacity of the

cathode at different N/P ratios. Due to the binder-free design and the replacement of Al foils, the energy density of NVPF-Ni-CF||Na-Sb-CC is higher than those calculated values of the conventional SMB when the areal capacity and the N/P ratio are the same.

2.5. Versatility of the self-regulating mechanism to other metal anodes

Very importantly, the self-regulating mechanism is suitable to protect other types of metal anodes. As metallic ions (such as Li^+, K^+) could form semiconducting compounds with NiSb, the self-regulating mechanism is also applicable to inhibit the dendrite growth of other metal anodes such as Li metal and K metal. As a proof of concept, we fabricated Li metal and K metal anodes on NiSb modified current collectors. Both metal anodes showed dendrite-free morphologies similar to that of the Na metal anode (Figure S22a and S22b). Owing to the self-regulating mechanism, the overpotential of the symmetrical cell of the Li metal anode on NiSb-CC (Li-NiSb-CC) was significantly reduced to 11.3 mV comparted with that of Li metal on CC (Li-CC, 20.7 mV, Figure S22c). Importantly, no fluctuation of the GCD profiles was observed in the symmetrical cells with Li-NiSb-CC, indicating a dendrites-free behavior during the plating and stripping. The symmetrical cell made of K metal on NiSb-CC (K-NiSb-CC) also displayed an significantly lower and flatter overpotential (~64 mV) than that made of K metal on pristine CC (K-CC, ~375 mV, Figure S22d). Li-NiSb-CC possessed a stable and flat GCD profiles for over 1,200 h under charging/discharging at 1C, while the Li-CC suffered from a dramatical increase in the overpotential after 300 h under the same testing conditions (Figure S22e). With the help of self-regulating NiSb interface, the K-NiSb-CC could stably cycle for over 500 h whereas cell with K-CC died after cycling for 12h (Figure S22f). As shown in Figure S22g, Li-NiSb-CC (3.5 mAh cm^{-2}) showed a much higher average CE of 99.8% than Li-CC (98.5%). The improvement of CE of the K metal anode (3.5 mAh cm^{-2}) was more prominent, from 92.0% to 99.7% (Figure S22h).

3. Conclusion

In conclusion, we have reported the discovery of the self-regulating mechanism of Na metal using an alloy interface NiSb. The NiSb, which was deposited on the surface of the current collector, reacted with Na^+ ions during the plating process and formed isolated Na_3Sb nano-islands and a continuous Ni matrix. Nano-sized Na metal seeds are firstly deposited on the sodiophilic Na_3Sb domains. The built-in electric field of the Na/Na_3Sb heterostructure hindered the subsequent growth of the Na seed. Instead, Na metal was deposited on the surface of the electron-favored conductive Ni matrix, which connected the nano seeds and flattened the Na metal layer.

We have demonstrated that applying this self-regulating NiSb interface on the 3D CC could yield high-capacity, dendrite-free, and long-cycle-life Na metal anodes. Importantly, this strategy could yield stable SMBs with remarkable energy densities over 200 Wh kg^{-1} with flooded electrolyte and over 230 Wh kg^{-1} with lean electrolyte, when all the cell weights were taken into consideration. Note that this is the first report which reaches the milestone of 200 Wh kg^{-1}, where Na batteries are more economical than Li batteries. We further demonstrate that this self-regulating mechanism is an universal strategy to protect other alkali metal anodes. Our findings show a great leap toward the realization of high-energy-density and sustainable Na batteries in grid storage.

4. Experimental Section/Methods

Preparation of Cu- or Ni-coated carbon cloth (CC)/carbon felt (CF) and amorphous Ni coated CC (aNi-CC): All the chemicals were purchased from Sigma-Aldrich without further purification. Commercially available hydrophobic CC (W0S1009, Taiwan CeTech Co. Ltd.) was first soaked and sonicated in a mixed solution of concentrated sulfuric acid and nitric acid (V_{H2SO4}/V_{HNO3}=3:1) for 2 h at 80 °C and then rinsed with the deionized (DI) water. After this process, the hydrophobic CC became hydrophilic. The hydrophilic CC was further coated with

Ni through a polymer assisted metal deposition (PAMD) process. In a typical PAMD process, the CC was first silanized by being immersed into a solution containing 4 % (v/v) [3-(methacryloyloxy)propyl]trimethoxysilane in a mixed solvent ($V_{ethanol}$:$V_{acetic\ acid}$: $V_{DI\ water}$=95:1:4) for 1 h at room temperature. After rinsing in the deionized (DI) water for several times, the silanized CC was further immersed in an aqueous solution of [2-(methacryloyloxy)ethyl]trimethyl ammonium chloride (METAC, 20 wt.%). Potassium persulfate (2 g L^{-1}) was added to initialize the polymerization of METAC at 80 °C. After 1 h, PMETAC-coated CC was further washed with DI water and then dipped into an aqueous solution of $(NH_4)_2PdCl_4$ (5 mM) in dark environment to load the catalyst on the surface. The residual $[PdCl_4]^{2-}$ was removed by washing in the DI water. Finally, the $[PdCl_4]^{2-}$ loaded CC were immersed into a mixed aqueous solution of A and B (pH=7.5) for 30 min, where solution A comprised of $NiSO_4 \cdot 6H_2O$ (80 g L^{-1}), sodium citrate (40 g L^{-1}), and lactic acid (20 g L^{-1}) and solution B was dimethylamine borane (1.5 g L^{-1}) in water. Ni-coated CF (CF, SQ-2000, Kunshan ShunDuoShun Electronic Materials) was made through the same procedure as the preparation of Ni-coated CC (Ni-CC). For Cu deposition, solution A was an aqueous solution comprised of NaOH (12 g L^{-1}), $CuSO_4 \cdot 5H_2O$ (13 g L^{-1}), and $KNaC_4H_4O_6 \cdot 4H_2O$ (29 g L^{-1}), and solution B was an aqueous solution of formaldehyde with a concentration of 9.5 mL L^{-1}. The preparation of aNi-CC was conducted according to the previous report[54]. Typically, the $[PdCl_4]^{2-}$ loaded CC was immersed into a solution containing $NiSO_4 \cdot 6H_2O$ (25 g/L), NaH_2PO_2 (20 g/L), $CH_3COONa \cdot 3H_2O$ (10 g/L) and $C_6H_5Na_3O_7 \cdot 2H_2O$ (10 g/L). The solution was heated to 90 °C under the stirring for 1h.

Preparation of NiSb-coated CC (NiSb-CC) and NiSb-coated Ni foil (NiSb-Ni): The Ni-CC was immersed into an ethanol solution containing antimony trichloride ($SbCl_3$, 2 g L^{-1}) and sealed in an autoclave, which was then heated to 85 °C for 4 h. The sample was then washed with ethanol 3 times. The NiSb-Ni foil was prepared through the same procedure.

Preparation of Sb coated Ni foil and CC(Sb-CC): The Sb-coated Ni foil was prepared via thermal evaporation (JSD-600). To prepare Sb-CC, $SbCl_3$ (10 mM) and tetrabutylammonium tetrafluoroborate (0.1 M) were dissolved in the dimethyl sulfoxide in the Ar environment as the bath solution. And then, the Cu-CC were immersed in the above solution for 24 h for the complete replacement of the Sb coatings.

Preparation of Na-CC, Na-Ni-CC, Na-NiSb-CC, Li-CC, Li-NiSb-CC, K-CC and K-NiSb-CC: The NiSb-CC was placed at the edge of the molten Na droplets at 300 °C and the Na could infuse into the NiSb-CC to obtain Na-NiSb-CC. The Na-CC and Na-Ni-CC were prepared by immersing the CC and Ni-CC in the molten Na. The preparation of Li-CC, Li-NiSb-CC, K-CC and K-NiSb-CC was following the similar procedures.

Preparation of NVPF cathode: Stoichiometric amounts of $NH_4H_2PO_4$, NaF and NH_4VO_3 (2 : 3 : 2, mole ratio) were dissolved in distilled water to form a pale-yellow solution. An aqueous citric acid (10% wt.) was dipped into the pale solution under the stirring until the color turned orange. The mixed solution was evaporated at 85 °C to form the precursor gel. The Ni-CF were immersed into the gel to load the precursors and then dried. The Ni-CF supported NVPF precursor was annealed in the Ar at 650 °C for 8 h to produce the binder-free NVPF-Ni-CF cathode. The loading of the NVPF on the Ni-CF can be adjusted by controlling the concentration of precursor gel.

Structural characterization: The morphology and the energy-dispersive X-ray mapping of the electrode were observed by the field emission scanning electron microscopy (FESEM, TESCAN MAIA3 and TESCAN VEGA3, Brno, Czech Republic). TEM images and SAED patterns were obtained on field emission scanning transmission microscopy (STEM, JEM-2100F, JEOL, Japan). The X-ray photoelectron spectroscopy (XPS, Axis Ultra, Kratos) was conducted using a monochromatic Al-Kα (1486.6 eV) excitation source. The contact angles were measured using the optical contact angle measuring instrument (SDC-350).

Electrochemical test: The electrochemical properties were investigated using coin cells and the electrolyte consisted of 1 M $NaClO_4$ in a mixture of ethylene carbonate (EC) and diethyl carbonate (DEC) with 5 wt.% fluorinated ethylene carbonates (FEC) as an additive (V_{EC}: V_{DEC}=1:1). A glass fiber film (Whatman, GF/C, 260 μm) was used as the separator. CR2025 coin cells were assembled in an argon-filled glove box with oxygen and moisture content lower than 0.1 ppm. For the cells tested under lean electrolyte conditions, the separator was Celgard 2500 and the electrolyte amount was 3 mg mAh^{-1}. For the assembling of the lithium ion coin cells, the electrolyte utilized was lithium bis((trifluoromethyl)sulfonyl)azanide (LiTFSI) with a concentration of 1M dissolved in a mixture of dimethoxyethane (DME) and dioxolane (DOL) added with 2 wt. % $LiNO_3$ (V_{DOL}:V_{DME}=1:1). The separator was Celgard 2500. The electrolyte for the plating and striping of potassium was potassium bis(fluorosulfonyl)amide dissolved in DME with a concentration of 1M. The separator for the potassium battery was glass fiber film (Whatman, GF/C, 260 μm). The cycling performance was evaluated using the Arbin and Neware battery testing systems. The energy density of the cell was calculated based on the mass of cell components including the current collectors, electrodes, separator, and the electrolyte.

In-situ obeservation of Na deposition: The in-situ electrochemical cell (model: STC-Q) was purchased from the MTI group and detailed information of the cell can be accessed through the website (https://www.mtixtl.com/PEEKSplitTestCellwithQuartzObservationWindowforin-situX-RayAnaly.aspx). The whole setup was schemetically illustrated in the Fig.S6. The counter electrode was the sodium metal and the working electrode was different foil. The electrolyte was the same in the section of electrochemical test. The in-situ cell was assembled in the glove box with the content of moisture and oxygen lower than 0.1 ppm and sealed with PTFE O rings. The whole cell was transferred out. The Na metal electrode was connected with the counter electrode and reference electrode. The working electrode was linked with the working electrode of the electrochemical workstation. The current provided by the

electrochemmical workstation (CHI 660e) was 1 mA cm^{-2}. And the optical microscopy images and videos were captured by NIKON Eclipse Ni-U.

COMSOL simulation: The model "Electrodeposition, Tertiary Nernst-Planck" was used to simulate the deposition process of Na. The simulation cell consisted of electrolyte with a thickness of 10 μm, Na electrode, Ni foil electrode, and the resultant Na_3Sb in the Ni matrix after the sedation of NiSb. The overpotential of deposition was set as -0.1 V vs Na/Na^+ at the working electrode. The diffusion coefficient of Na^+ in the electrolyte was determined by the $\sigma_i=\mu_i ne$. The conductivity of the electrolyte (1.0 M $NaClO_4$ in EC: DEC=1:1 vol.% with 5.0 wt.% FEC) was 6.8 mS cm^{-1} according to the data provided by the Guangdong Canrd New Energy Technology Co., Ltd and the mobility of Na was 6.8×10^{-5} cm^2 s^{-1}. The Passion equation initially determined the potential on the surface of Na_3Sb and Na seeds. And the interfaces between the Na metal and Na_3Sb nano islands were set as the Schottky contacts. The flux of Na^+ ions in the liquid electrolyte was given by the Nernst-Planck equation:

$$\boldsymbol{N}_i = -D_i\nabla c_i - z_i u_i F c_i \nabla\varphi \quad (2)$$

Where $\boldsymbol{N}_i$ denoted the transport vector (mol $m^{-2}\cdot s^{-1}$), c_i represented the concentration in the electrolyte (mol L^{-1}), z_i was the charge for the ionic species, u_i was the mobility of the charged species (m^2 s^{-1}), F was Faraday's constant (26.801 A·h mol^{-1}), and φ was the local potential in the electrolyte.

The following equation determined the ion migration of the electric field:

$$\frac{\partial c_i}{\partial t} + \nabla\cdot\boldsymbol{N}_i = 0 \quad (3)$$

Where c_i represented the concentration of Na^+ or ClO_4^- (i=1 or 2). t was the time. The Butler-Volmer equation gives the boundary conditions on the anode and cathode for Na deposition and dissolution. The initial concentrations for Na^+ and ClO_4^- ions were 1 M. The electrodeposition and dissolution of Na on the working electrode and anode could be described using the following equations:

$$Na^+ + e^- \leftrightarrow Na \quad (4)$$

The other boundaries were insulating for the Na^+ and the flux of ClO_4^- was set as 0 on all the boundaries.

Supporting Information

Supporting Information is available from the Wiley Online Library or from the author.

Acknowledgements

L.W. and J.S. contributed equally to this work. The authors acknowledge the financial support from Shenzhen Municipal Science and Technology Innovation Commission (A0030246). The authors also acknowledge the technical supports from the Materials Research Centre (MRC) and Centre for Electron Microscopy (CEM) in the HongKong Polytechnic University.

Conflict of Interests

The authors declare no competing interests

Received: ((will be filled in by the editorial staff))
Revised: ((will be filled in by the editorial staff))
Published online: ((will be filled in by the editorial staff))

References

[1] N. Yabuuchi, M. Kajiyama, J. Iwatate, H. Nishikawa, S. Hitomi, R. Okuyama, R. Usui, Y. Yamada, S. Komaba, *Nat. Mater.* **2012**, *11*, 512.

[2] B. Dunn, H. Kamath, J.-M. Tarascon, *Science* **2011**, *334*, 928.

[3] S. Spillias, P. Kareiva, M. Ruckelshaus, E. McDonald-Madden, *Nat. Clim. Change* **2020**, *10*, 974.

[4] T. Liu, Y. Zhang, Z. Jiang, X. Zeng, J. Ji, Z. Li, X. Gao, M. Sun, Z. Lin, M. Ling, J. Zheng, C. Liang, *Energy Environ. Sci.* **2019**, *12*, 1512.

[5] BloomburgNEF, New Energy Outlook 2020, https://about.bnef.com/new-energy-outlook/, accessed: Dec. **2020**.

[6] W. Z. Cao, J. N. Zhang, H. Li, *Energy Storage Mater.* **2020**, *26*, 46.

[7] X. Zhu, L. Wang, *EcoMat* **2020**, *2*, e12043.

[8] J. Lang, Y. Jin, K. Liu, Y. Long, H. Zhang, L. Qi, H. Wu, Y. Cui, *Nat. Sustain.* **2020**, *3*, 386.

[9] H. S. Hirsh, Y. X. Li, D. H. S. Tan, M. H. Zhang, E. Y. Zhao, Y. S. Meng, *Adv. Energy Mater.* **2020**, *10*, 2001274.

[10] C. Zhao, Q. Wang, Z. Yao, J. Wang, B. Sánchez-Lengeling, F. Ding, X. Qi, Y. Lu, X. Bai, B. Li, H. Li, A. Aspuru-Guzik, X. Huang, C. Delmas, M. Wagemaker, L. Chen, Y.-S. Hu, *Science* **2020**, *370*, 708.

[11] M. Lee, J. Hong, J. Lopez, Y. Sun, D. Feng, K. Lim, W. C. Chueh, M. F. Toney, Y. Cui, Z. Bao, *Nat. Energy* **2017**, *2*, 861.

[12] C. Vaalma, D. Buchholz, M. Weil, S. Passerini, *Nat. Rev. Mater.* **2018**, *3*, 18013.

[13] D. Karabelli, S. Singh, S. Kiemel, J. Koller, A. Konarov, F. Stubhan, R. Miehe, M. Weeber, Z. Bakenov, K. P. Birke, *Front. Energy Res.* **2020**, *8*, 349.

[14] E. Goikolea, V. Palomares, S. Wang, I. R. de Larramendi, X. Guo, G. Wang, T. Rojo, *Adv. Energy Mater.* **2020**, *10*, 2002055.

[15] Y. He, P. Xu, B. Zhang, Y. Du, B. Song, X. Han, H. Peng, *ACS Appl. Mater. Interfaces* **2017**, *9*, 38401.

[16] L. Wang, X. Li, Z. Jin, Z. Liang, X. Peng, X. Ren, B. Gao, G. Feng, P. K. Chu, K. Huo, *J. Mater. Chem. A* **2019**, *7*, 27475.

[17] Z. Liu, T. Lu, T. Song, X.-Y. Yu, X. W. Lou, U. Paik, *Energy Environ. Sci.* **2017**, *10*, 1576.

[18] Y. Wen, K. He, Y. Zhu, F. Han, Y. Xu, I. Matsuda, Y. Ishii, J. Cumings, C. Wang, *Nat. Commun.* **2014**, *5*, 4033.

[19] S. Alvin, D. Yoon, C. Chandra, R. F. Susanti, W. Chang, C. Ryu, J. Kim, *J. Power Sources* **2019**, *430*, 157.

[20] A. Sarkar, C. V. Manohar, S. Mitra, *Nano Energy* **2020**, *70*, 104520.

[21] P. Santhoshkumar, N. Shaji, M. Nanthagopal, J. W. Park, C. Senthil, C. W. Lee, *J. Power Sources* **2020**, *470*, 228459.

[22] T. Palaniselvam, M. Goktas, B. Anothumakkool, Y.-N. Sun, R. Schmuch, L. Zhao, B.-H. Han, M. Winter, P. Adelhelm, *Adv. Funct. Mater.* **2019**, *29*, 1900790.

[23] W. Tian, S. Zhang, C. Huo, D. Zhu, Q. Li, L. Wang, X. Ren, L. Xie, S. Guo, P. K. Chu, H. Zeng, K. Huo, *ACS Nano* **2018**, *12*, 1887.

[24] Y. X. Wang, Y. X. Wang, Y. X. Wang, X. M. Feng, W. H. Chen, X. P. Ai, H. X. Yang, Y. L. Cao, *Chem* **2019**, *5*, 2547.

[25] K. M. Abraham, *ACS Energy Lett.* **2020**, *5*, 3544.

[26] A. Bauer, J. Song, S. Vail, W. Pan, J. Barker, Y. Lu, *Adv. Energy Mater.* **2018**, *8*, 1702869.

[27] B. Lee, E. Paek, D. Mitlin, S. W. Lee, *Chem. Rev.* **2019**, *119*, 5416.

[28] L. Ye, M. Liao, T. Zhao, H. Sun, Y. Zhao, X. Sun, B. Wang, H. Peng, *Angew. Chem. Int. Ed.* **2019**, *58*, 17054.

[29] T. Yang, T. Qian, Y. Sun, J. Zhong, F. Rosei, C. Yan, *Nano Lett.* **2019**, *19*, 7827.

[30] Z. W. Seh, J. Sun, Y. Sun, Y. Cui, *ACS Cent. Sci.* **2015**, *1*, 449.

[31] H. Wang, C. Wang, E. Matios, W. Li, *Angew. Chem. Int. Ed.* **2018**, *57*, 7734.

[32] D. A. Rakov, F. Chen, S. A. Ferdousi, H. Li, T. Pathirana, A. N. Simonov, P. C. Howlett, R. Atkin, M. Forsyth, *Nat. Mater.* **2020**, *19*, 1096.

[33] M. Zhu, G. Wang, X. Liu, B. Guo, G. Xu, Z. Huang, M. Wu, H.-K. Liu, S.-X. Dou, C. Wu, *Angew. Chem. Int. Ed.* **2020**, *59*, 6596.

[34] S. Tang, Y. Y. Zhang, X. G. Zhang, J. T. Li, X. Y. Wang, J. W. Yan, D. Y. Wu, M. S. Zheng, Q. F. Dong, B. W. Mao, *Adv. Mater.* **2019**, *31*, 1807495.

[35] S.-S. Chi, X.-G. Qi, Y.-S. Hu, L.-Z. Fan, *Adv. Energy Mater.* **2018**, *8*, 1702764.

[36] Z. Xu, J. Yang, T. Zhang, L. Sun, Y. Nuli, J. Wang, S.-i. Hirano, *Adv. Funct. Mater.* **2019**, *29*, 1901924.

[37] H. Gao, S. Xin, L. Xue, J. B. Goodenough, *Chem* **2018**, *4*, 833.

[38] H. Sun, G. Zhu, X. Xu, M. Liao, Y.-Y. Li, M. Angell, M. Gu, Y. Zhu, W. H. Hung, J. Li, Y. Kuang, Y. Meng, M.-C. Lin, H. Peng, H. Dai, *Nat. Commun.* **2019**, *10*, 3302.

[39] D. Lei, Y.-B. He, H. Huang, Y. Yuan, G. Zhong, Q. Zhao, X. Hao, D. Zhang, C. Lai, S. Zhang, J. Ma, Y. Wei, Q. Yu, W. Lv, Y. Yu, B. Li, Q.-H. Yang, Y. Yang, J. Lu, F. Kang, *Nat. Commun.* **2019**, *10*, 4244.

[40] S. Jiao, J. Zheng, Q. Li, X. Li, M. H. Engelhard, R. Cao, J.-G. Zhang, W. Xu, *Joule* **2018**, *2*, 110.

[41] B. Sun, P. Xiong, U. Maitra, D. Langsdorf, K. Yan, C. Wang, J. Janek, D. Schröder, G. Wang, *Adv. Mater.* **2020**, *32*, 1903891.

[42] H. Wang, E. Matios, J. Luo, W. Li, *Chem. Soc. Rev.* **2020**, *49*, 3783.

[43] X. Lu, J. Luo, E. Matios, Y. Zhang, H. Wang, X. Hu, C. Wang, H. Wang, J. Wang, W. Li, *Nano Energy* **2020**, *69*, 104446.

[44] S. Tang, Y.-Y. Zhang, X.-G. Zhang, J.-T. Li, X.-Y. Wang, J.-W. Yan, D.-Y. Wu, M.-S. Zheng, Q.-F. Dong, B.-W. Mao, *Adv. Mater.* **2019**, *31*, 1807495.

[45] X.-M. Zheng, J.-H. You, J.-J. Fan, G.-P. Tu, W.-Q. Rong, W.-J. Li, Y.-X. Wang, S. Tao, P.-Y. Zhang, S.-Y. Zhang, S.-Y. Shen, J.-T. Li, L. Huang, S.-G. Sun, *Nano Energy* **2020**, *77*, 105123.

[46] S. Dong, C. Li, L. Yin, *Eur. J. Inorg. Chem.* **2018**, *2018*, 992.

[47] J. Liu, Z. Yang, J. Wang, L. Gu, J. Maier, Y. Yu, *Nano Energy* **2015**, *16*, 389.

[48] A. R. H. F. Ettema, R. A. de Groot, *Phys. Rev. B* **2000**, *61*, 10035.

[49] J. Chang, J. Shang, Y. M. Sun, L. K. Ono, D. R. Wang, Z. J. Ma, Q. Y. Huang, D. D. Chen, G. Q. Liu, Y. Cui, Y. B. Qi, Z. J. Zheng, *Nat. Commun.* **2018**, *9*, 4480.

[50] K. N. Wood, M. Noked, N. P. Dasgupta, *ACS Energy Lett.* **2017**, *2*, 664.

[51] G. Yan, S. Mariyappan, G. Rousse, Q. Jacquet, M. Deschamps, R. David, B. Mirvaux, J. W. Freeland, J.-M. Tarascon, *Nat. Commun.* **2019**, *10*, 585.

[52] K. Chayambuka, G. Mulder, D. L. Danilov, P. H. L. Notten, *Adv. Energy Mater.* **2018**, *8*, 1800079.

[53] A. Eftekhari, *Sustain. Energy Fuels* **2017**, *1*, 2053.

[54] Y. Tan, Y. Zhang, X. Wang, L. Zeng, F. Luo, A. Liu, *J. Electroanal. Chem.* **2020**, *856*, 113739.

A self-regulating alloy interface, which contains chemically sodiophilic yet electron-hindered semiconducting Na_3Sb nano-islands and the sodiophobic yet electron-favored conductive Ni matrix, is reported. Benifiting from the unique self-regulating mechanism and textile structured current collector, full cells paired with high-capacity cathode delivers a ultrahigh energy density exceeding 200 Wh kg^{-1} with ultrahigh energy efficiency of 95.8%.

L. Wang, J. Shang, Q. Huang, H. Hu, Y. Zhang, C. Xie, Y. Luo, Y. Gao, H. Wang, Z. Zheng*

Smoothing sodium metal anode with a self-regulating alloy interface for high-energy and sustainable sodium metal battery

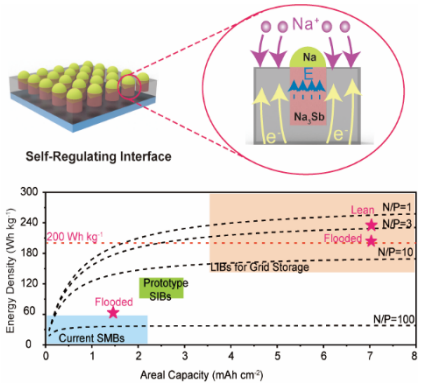

Supporting Information

Smoothing sodium metal anode with a self-regulating alloy interface for high-energy sodium metal battery

*Lei Wang, Jian Shang, Qiyao Huang, Hong Hu, Yuqi Zhang, Chuan Xie, Yufeng Luo, Yuan Gao, Huixin Wang, Zijian Zheng**

Dr. L. Wang, Dr. J. Shang, Prof. Q. Huang, Dr. H. Hu, Dr. Y. Zhang, X. Chuan, Dr. Y. Luo, Dr. Y. Gao, H. Wang, Prof. Z. Zheng
Laboratory for Advanced Interfacial Materials and Devices, Research Centre for Smart Wearable Technology, Institute of Textiles and Clothing, The Hong Kong Polytechnic University, Hong Kong SAR, China
E-mail: tczzheng@polyu.edu.hk

Prof. Z. Zheng
Research Institute for Smart Energy, The Hong Kong Polytechnic University, Hong Kong SAR, China

Supporting text 1:

The estimation of the effective surface area (EASA) of the carbon cloth

If we assume that the fiber in the carbon cloth is cylindrical with a radius of *r,* then the mass *m* of the fiber with the length of *l* can be calculated:

$$m = \rho V = \rho \pi r^2 l \quad (1)$$

where V is the volume of the fiber and ρ is the density of the carbon fiber.

Then the length of the carbon fiber in the carbon cloth can be described as:

$$l = \frac{m}{\rho \pi r^2} \quad (2)$$

Then the lateral surface area:

$$S = 2\pi r l = \frac{2m}{\rho r} \quad (3)$$

For carbon cloth used in this work, its areal mass is 12 mg cm^{-2}, the average radius of the carbon fiber is 4 μm (Figure S5a and S5b), and the density of the carbon fiber is about 1.75 g cm^{-3}. Therefore, the surface area of the carbon cloth with a projected area of 1 cm^2 can be estimated to be:

$$S = \frac{2m}{\rho r} = 34.2 \text{ cm}^2 \quad (4)$$

Note that this result is obtained without considering the base surface area, the roughness of the lateral surface, and the shape change during the spinning and weaving of the fibers in the preparation process of the carbon cloth. As a result, in real conditions, the effective area should be **larger** than this value.

We also employed an electrochemical method to evaluate the effective area of the carbon cloth. The carbon cloth was assembled into a coin cell as the working electrode to test its electrochemical double-layer capacitance. CV tests were conducted at different scan rates (Figure S5c), and the fitting line of the resulting current density at the potential of 2.3 V was plotted in Figure S5d. A specific capacitance (C_{dl}) of 901 μF could be obtained. As the ideal

capacitance for the carbon surface (C_{ref}) [1-2] is 21 μF cm^{-2}, EASA of the carbon cloth with a projected area of 1 cm^2 in the coin cell could be estimated to be:

$$EASA = \frac{C_{dl}}{C_{ref}} = 42.9 \text{ cm}^2 \quad (5)$$

Supporting text 2:

The estimation of the theoretical energy density of the conventional sodium metal battery (SMB)

If we assume the total utilization of the active materials in cathode, the energy density of the cell with the designed capacity (C) can be estimated according to the equation (6):

$$E = \frac{\bar{U}C}{m} = \frac{\bar{U}C}{\frac{xC}{C_a}+\frac{C}{C_c}+m_{in}} = \frac{\bar{U}}{\frac{x}{C_a}+\frac{1}{C_c}+\frac{m_{in}}{C}} \quad (6)$$

where $\bar{U}$ is the average potential for the discharge process, C_a and C_c are the theoretical capacity for the anode and cathode. x is the area capacity ratio of negative to positive electrodes (N/P ratio). m is the mass of the cells, including the mass of active materials in electrodes and the mass of the inactive components in the battery (m_{in}). In a conventional SMBs, the inactive components consist of the conductive additive, electrolyte, binder, and package materials.

Referring to the structure of the lithium-ion battery, conventional SMB composes of cathode, metallic anode, separator, and electrolyte. The cathode is a film, which consists of active materials, conductive additives, and binder that are coated on the surface of Al current collector. The mass ratio for the active materials to the binders and additives is 4 ($m_{\text{active materials}}$: $m_{\text{conductive additives}}$: m_{binder}=8:1:1). Al foil as current collectors for both cathode and anode electrodes of SMB weighs 8 mg cm^{-2}. The weight of the Celgard 2500 is 1 mg cm^{-2}. In our case, the theoretical capacities of the sodium-vanadium fluorophosphate (NVPF) and sodium (Na) are 128 mAh g^{-1} and 1165 mAh g^{-1}, and the average working potential for the NVPF is 3.8 V. The amount of electrolyte in the cell is 3 mg mAh^{-1}. In a large battery in the grid storage, the mass of the package can be ignored.

We then compare the energy density of the practical SMBs with our results. We also put the energy density of the previously reported SMBs in Figure 5d. The energy density of the cell increases with the rising of the areal capacity at various N/P ratios. In our case, the battery with the areal capacity of 1.49 mAh cm^{-2} can deliver an energy density of ~60 Wh kg^{-1}. As the areal

capacity reaches 7 mAh cm^{-2}, the energy density of the cell increases over 200 Wh kg^{-1}, which is about two folds higher than that of the current prototype sodium-ion batteries (SIBs).

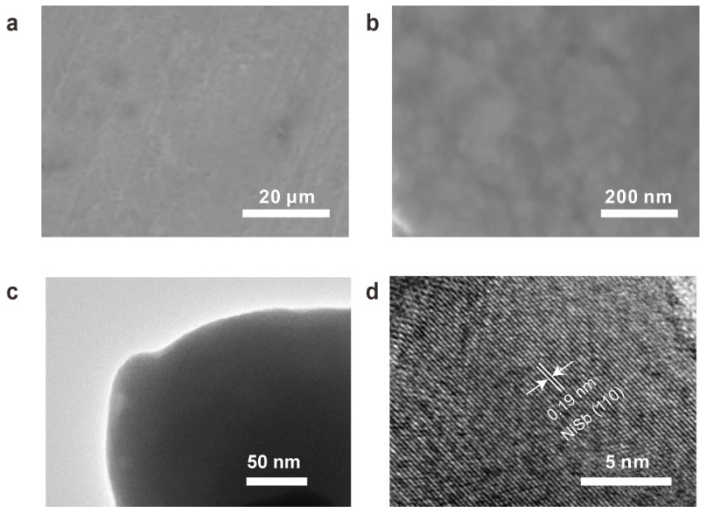

Figure S1. Morphology of the NiSb-coated Ni foil. a-b) Scanning electron microscopy (SEM) images of the NiSb-coated Ni foil under different magnifications. c) Low-magnification transmission electron microscope (TEM) image of the NiSb. d) High-resolution TEM image of NiSb. The lattices with the spacing of 0.19 nm correspond to the (110) plane of the NiSb.

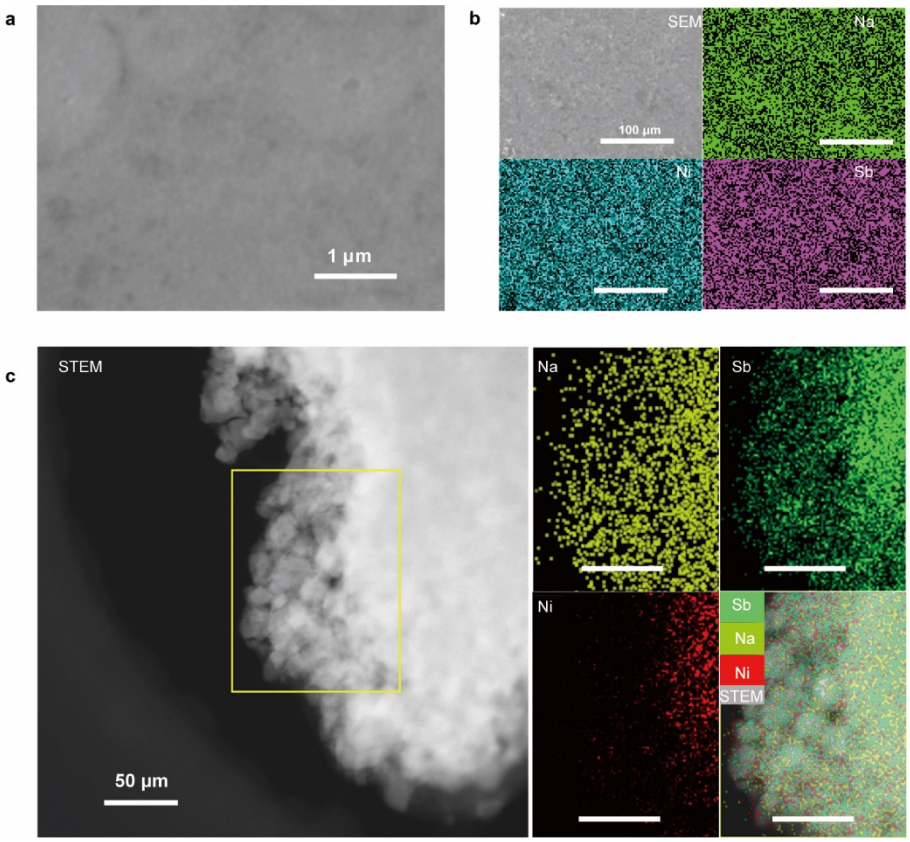

Figure S2. Morphology of the sodiated NiSb on Ni foil. a-b) SEM images of the sodiated NiSb on Ni foil under different magnifications. The sodiated NiSb on Ni foil shows a smooth surface. The EDS mapping demonstrates an even distribution of Ni and Na_3Sb generated during the sodiation process. c) STEM image and corresponding elemental mapping of the sodiated NiSb, demonstrating that the Na_3Sb was embedded in the Ni matrix.

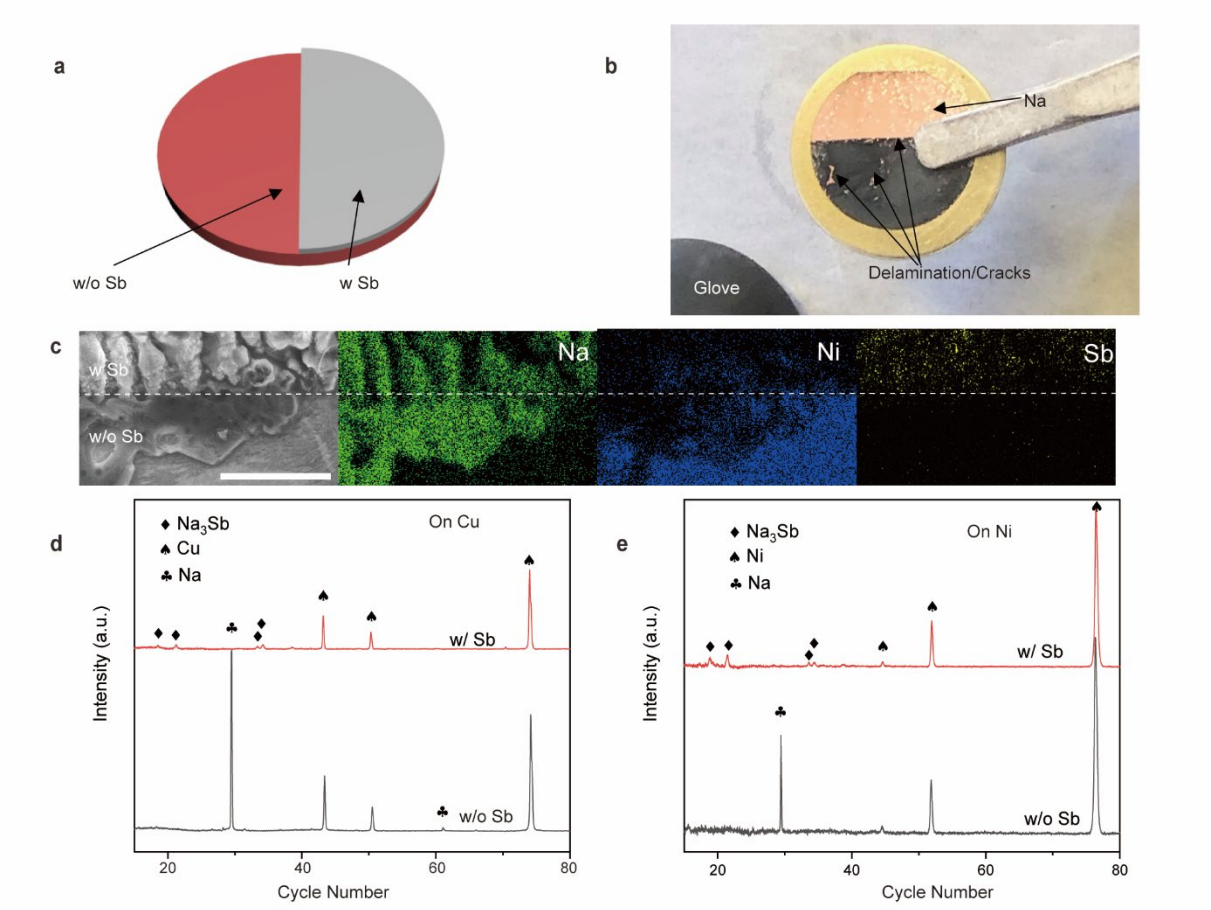

Figure S3. Direct evidence of the effect of the semiconducting Na_3Sb on the sodium deposition. a) a scheme of the designed electrode where half of the current collector was modified with Sb. b) the optical microscopy of the designed Cu electrode with deposition of Na at the capacity of 0.1 mAh cm^{-2}. Some shinning metallic Na could be observed on the bare Cu side, while only some delamination or the crack of Na_3Sb could be observed on the side modified with Sb. c) the SEM image and the EDS mapping of the Ni electrode with deposition of Na at the capacity of 0.1 mAh cm^{-2}. Metallic Na could be observed on the Ni side without Sb coating and only some Na embryo could be observed on the side with Sb coating. The scale bar in the figure represents 40 μm. d-e) the XRD spectrums for the side with/without Sb coatings. The electrode after deposition was split into two parts. On the side without the Sb coating, the signals of metallic Na could be detected while on the side whith the Sb modification, only the phase of Na_3Sb could be detected because the amount of Na on the Sb side was below the limit of detection for XRD measurements. This phenomenon could be observed on the both Cu electrode and Ni electrode. And the differences of the Na depositions on the two sides was beyound the sodiaphilicity and could be well explained by the semiconducting properties of Na_3Sb. The signal of the crystalline Ni comes from the commercially available Ni foil.

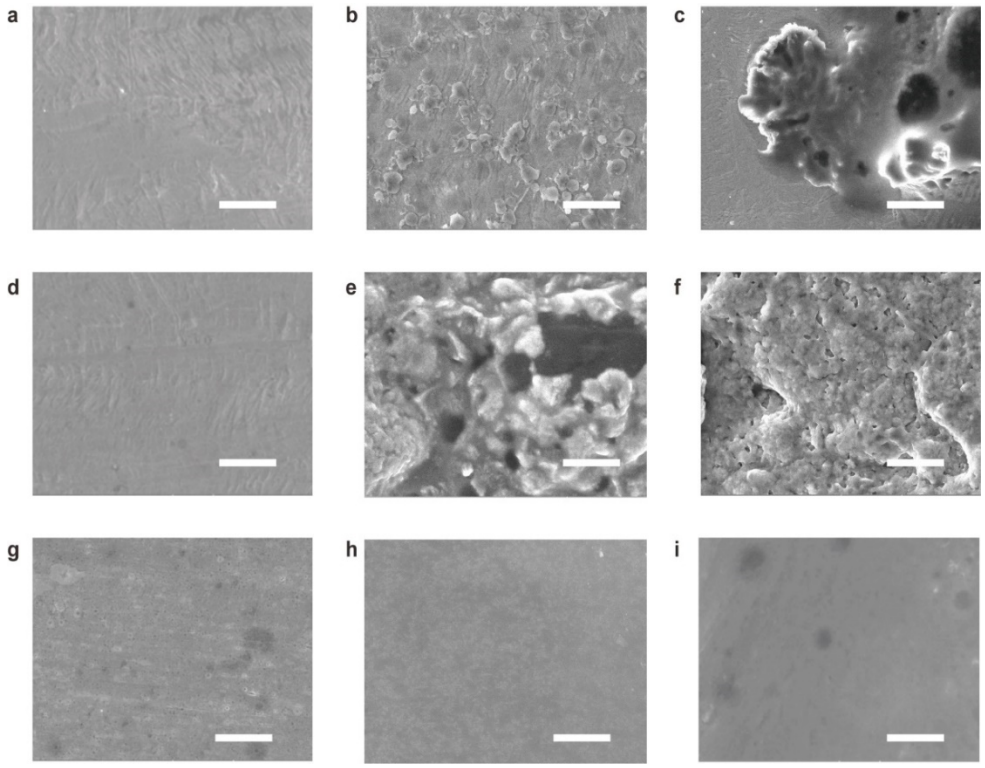

Figure S4. Na deposition on different current collectors at different capacities. a) SEM image of the Ni foil. b) SEM image of the Na nucleus on the Ni foil with a capacity of 0.1 mAh cm^{-2}. The distribution of the Na nucleus is not uniform. c) SEM image of the Na dendrite on the Ni foil with the capacity of 0.5 mAh cm^{-2}. Some Na nucleus merge into large dendrites. d) SEM image of the pristine Sb coated Ni foil. e) SEM image of the Na nucleus on the Ni foil with a capacity of 0.1 mAh cm^{-2}. The Sb coating is broken and partially detached from the Ni current collector during the plating process. Na prefers to deposit on the Sb. The distribution of the Na nucleus is not uniform. f) SEM image of the Na on the Ni foil with a capacity of 0.5 mAh cm^{-2}. The deposited Na showed a porous structure. g) SEM image of the pristine NiSb-coated Ni foil. h) SEM image of the Na nucleus on the NiSb-coated Ni foil with a capacity of 0.1 mAh cm^{-2}. i) SEM image of the Na film on the NiSb-coated Ni foil with a capacity of 0.5 mAh cm^{-2}. (Scale bar: 20 μm).

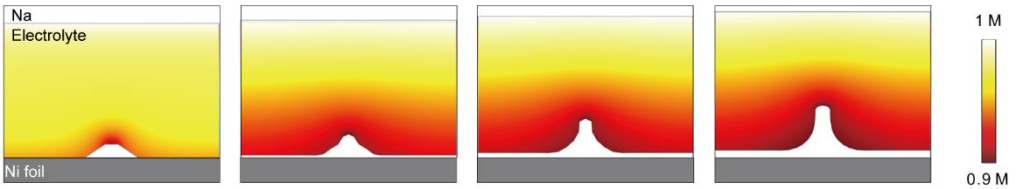

Figure S5. COMSOL simulation of the Na plating on the Ni foil. One large apex on the Ni foil quickly grows to a large Na dendrite

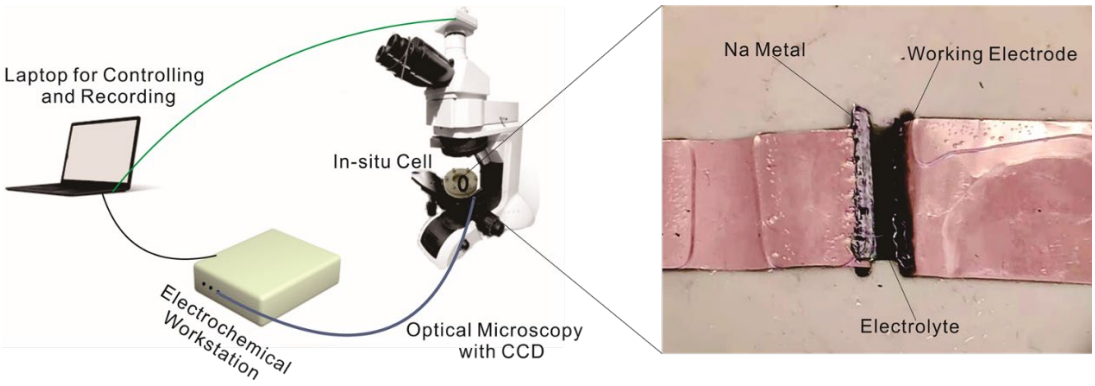

Figure S6. Illustration of setup for the in-situ observation of electrochemical deposition of Na.

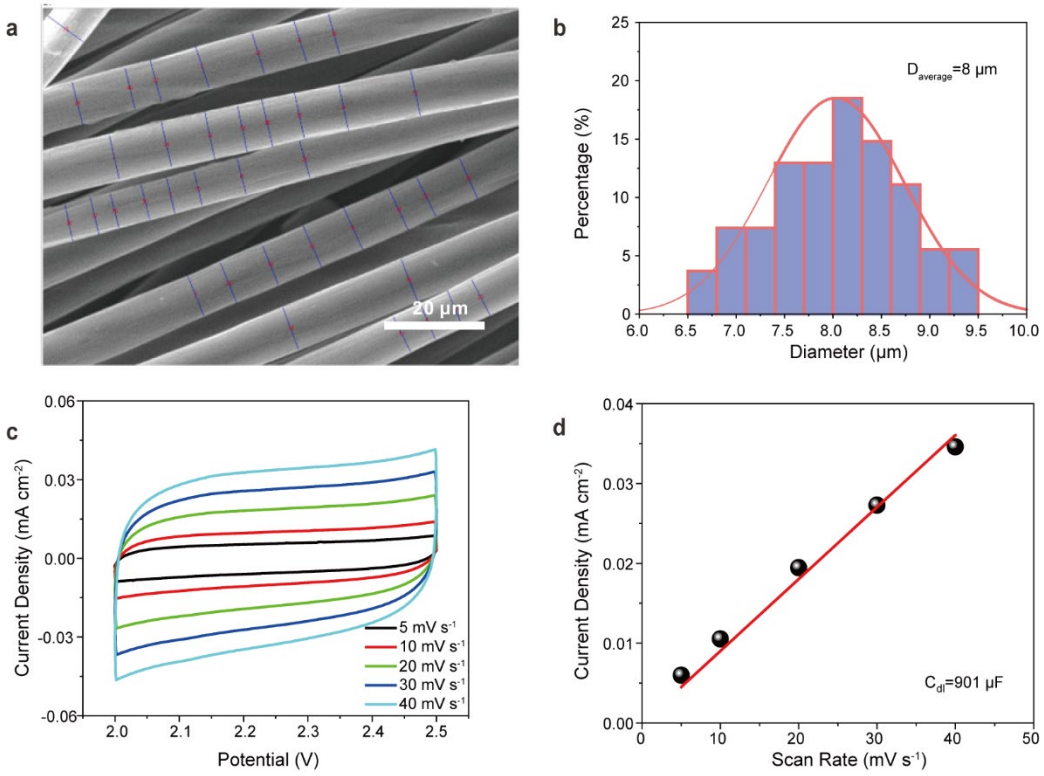

Figure S7. Estimation of the electrochemically active surface area of the CC. a) SEM image of the CC. The blue lines are at the measuring positions of the fiber diameters. b) Distribution of diameters of the fibers in the yarns in a. The average diameter of fibers in CC is ~8 μm. c) Cyclic voltammetry profiles of the CC with different san rates. These profiles exhibit rectangular shapes, demonstrating CC only displays electric-double-layer-capacitor (EDLC) charge storage behavior in the potential window of 2.0-2.5 V vs. Na/Na^+. d) Line fitting between the current density and scan rate. The slop is estimated to be 901 μF for the CC with a projected area of 1 cm^2.

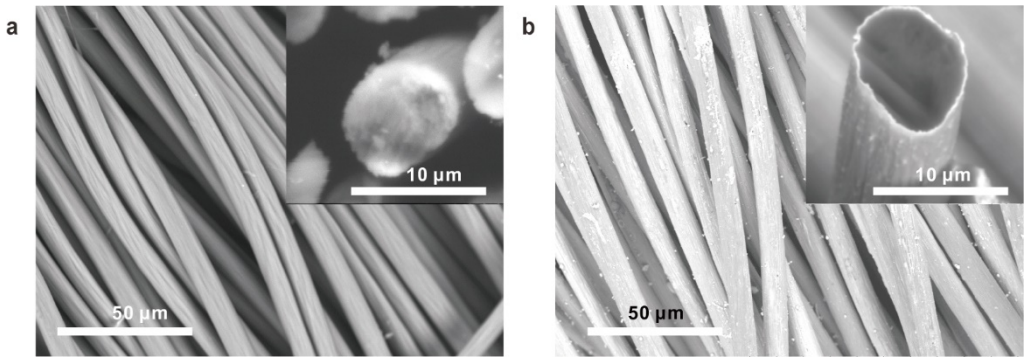

Figure S8. Morphology of the CC and Ni-CC. a) SEM image of the pristine CC. b) SEM image of Ni-CC. The inserts in the two figures are the cross-sectional SEM images of the single fiber in corresponding fabrics, indicating that a thin layer of Ni is coated on the CC after the polymer assisted metal deposition (PAMD) process.

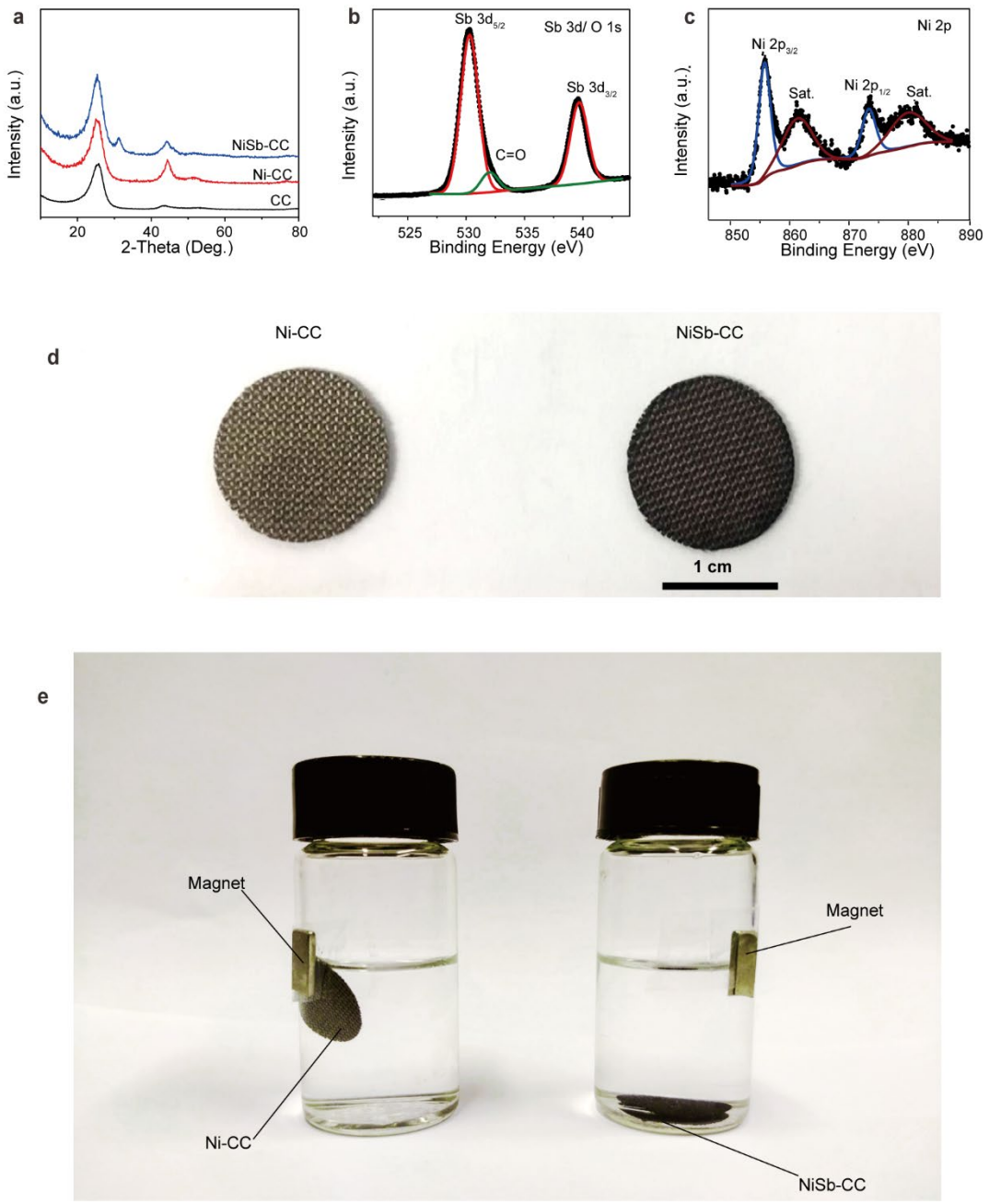

Figure S9. The phase transition from the CC to NiSb-CC. a) XRD spectrums for the pristine CC, Ni-CC and NiSb-CC. The pristine CC has two broad peaks at 26.3° and 44.3°, which can be indexed to the (002) and (101) lattice plane of the graphite. For Ni-CC, three new peaks at 44.5°, 51.8°, and 76.3° suggests the cubic Ni (JCPDS PDF#:04-0850). For NiSb, New peaks appeared at the position of 31.4°, 34.7°, 43.9°, and 46.2°, referring that the Ni turned transformed entirely to the NiSb (JCPDS PDF#:41-1439). The signal of crystalline Ni comes from the Ni coatings obtained after the polymer assisted metal deposition (PAMD). b) the fine spectrum for the Sb 3d in NiSb-CC. Two distinct peaks at 530.25 and 539.25 eV can attribute to the $3d_{5/2}$ and $3d_{3/2}$ signal in the NiSb[3-4]. c) the fine spectrum for the Ni 2p in NiSb-CC. Peaks emerged at the position of 855.5 eV and 873.0 eV and two accompanying satellite peaks arise at the binding energy of 879.7 and 861.8 eV [5]. d) The optical image for Ni-CC and NiSb-CC. e) Interaction between the Ni-CC, NiSb-CC with the magnet. The loss of the ferromagnetism demonstrates the complete conversion from Ni to NiSb in the composite.

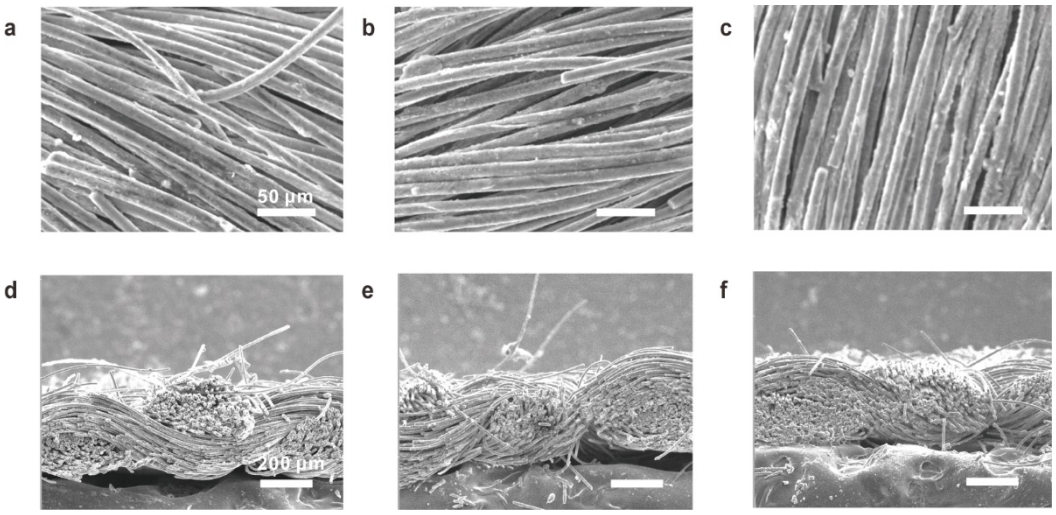

Figure S10. Morphology of the NiSb-CC electrochemically deposited with different amounts of Na. The top-down SEM images of Na-NiSb-CC electrodes with different capacitie.: a) 6 mAh cm^{-2}. b) 10 mAh cm^{-2}. c) 20 mAh cm^{-2}. The corresponding cross-sectional SEM images of Na-NiSb-CC electrodes with different capacities: d) 6 mAh cm^{-2}. e) 10 mAh cm^{-2}. f) 20 mAh cm^{-2}. Na prefers to deposit on the surface of fibers and the internal voids in CC was almost occupied. The woven structure of the CC remains during the process of deposition.

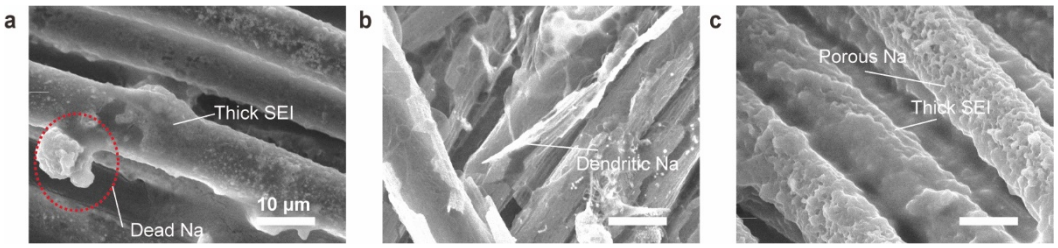

Figure S11. Morphology of the various hosts after evaluation of Coulombic efficiency (CE). a) CC. b) Ni-CC. c) Sb-CC. The thick layer of SEI can be found on CC and Sb-CC. Porous and dendritic structures can be observed on Ni-CC and CC.

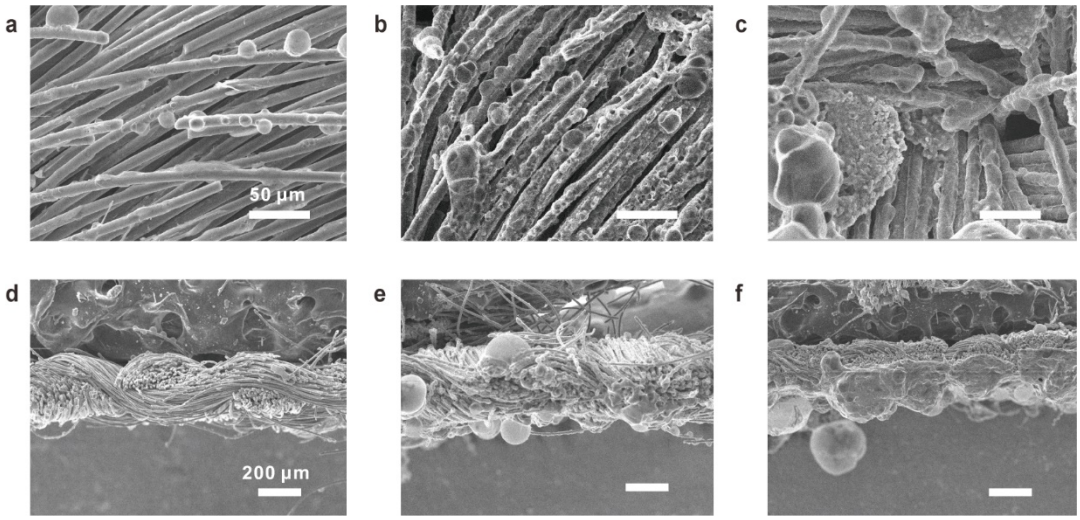

Figure S12. Morphology of CC electrochemically deposited with different amounts of Na. The top-down SEM images of Na-CC electrodes with different capacities: a) 3 mAh cm^{-2}. b) 6 mAh cm^{-2}. c) 10 mAh cm^{-2}. The corresponding cross-sectional images of Na-CC electrodes with different capacities: d) 3 mAh cm^{-2}. e) 6 mAh cm^{-2}. f) 10 mAh cm^{-2}. Large blocks of Na prefer to deposit on the surface of CC.

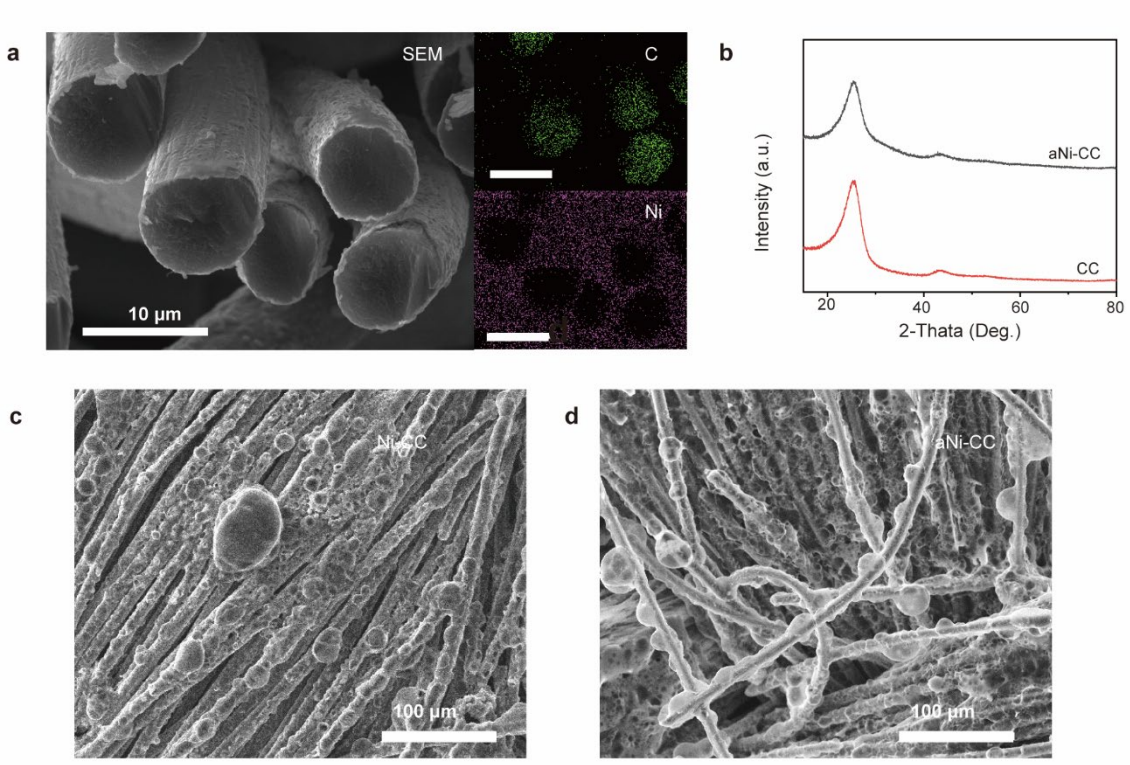

Figure S13. The preparation of the amorphous Ni coated CC (aNi-CC) and the corresponding electrochemical performance. a) The cross-sectional image and EDS mapping of the aNi-CC. b) XRD spectrums of the CC and aNi-CC. The morphology of the polycrystalline Ni coated CC (c, Ni-CC) and aNi-CC (d) after deposition of Na with the capacity of 4 mAh cm^{-2}.

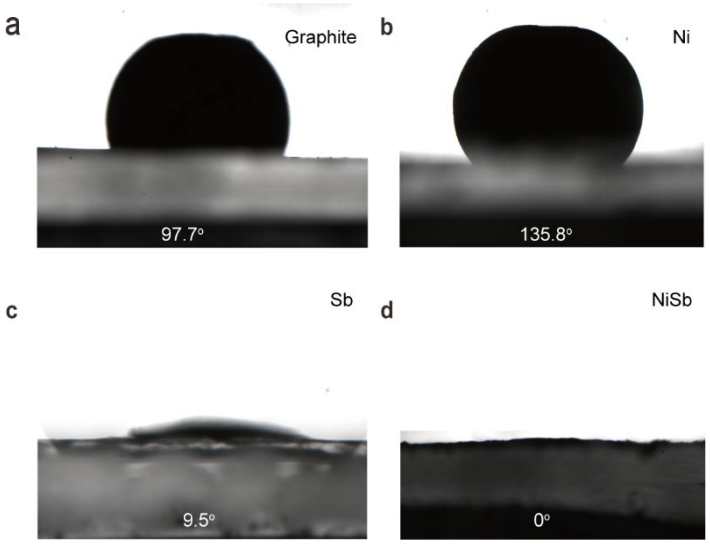

Figure S14. Contact angle of molten Na to different substrates. a) graphite. b) Ni foil. c) Sb coated Ni foil. d) NiSb-coated Ni foil. NiSb showed an improved wettability to molten Na.

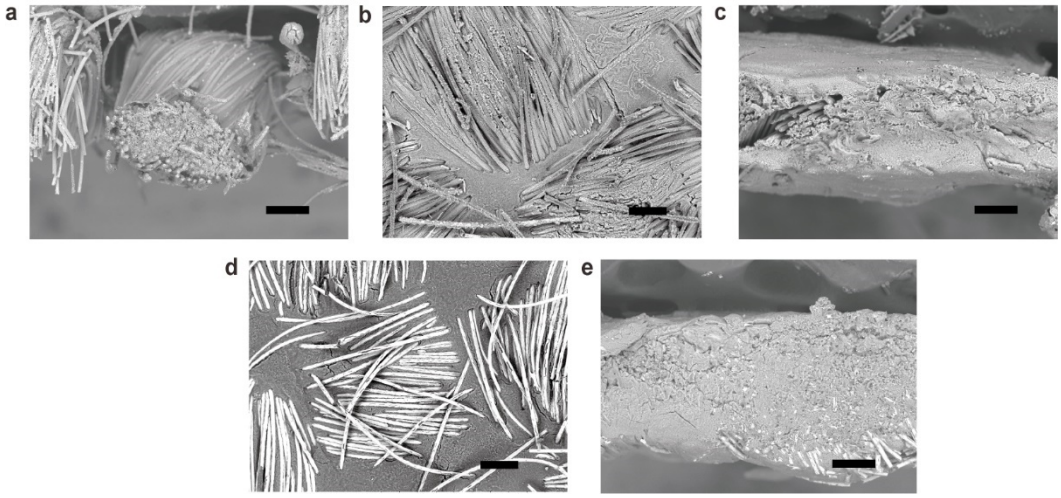

Figure S15. Morphology of the Na composite: a) Cross-sectional SEM image of the Na-NiSb-CC. Na only fills the space within the yarns of the NiSb-CC during the infusion process. Therefore, the loading of Na can be restricted to 18 mg cm^{-2}. b) Top-down SEM image of the Na-CC. A large amount of the Na gathers in the gaps between the yarns. The molten Na does not wet the fibers on the composite due to the poor sodiophilicity of CC. c) Cross-sectional SEM image of Na-CC. The molten Na does not wet some fibers inside the composite. d) Top-down SEM image of the Na-Ni-CC. A large amount of the Na gathers in the gaps between the yarns. The molten Na does not wet the fibers on the composite due to the poor sodiophilicity. e) Cross-sectional SEM images for the Na-Ni-CC. (Scale bars: 100 μm).

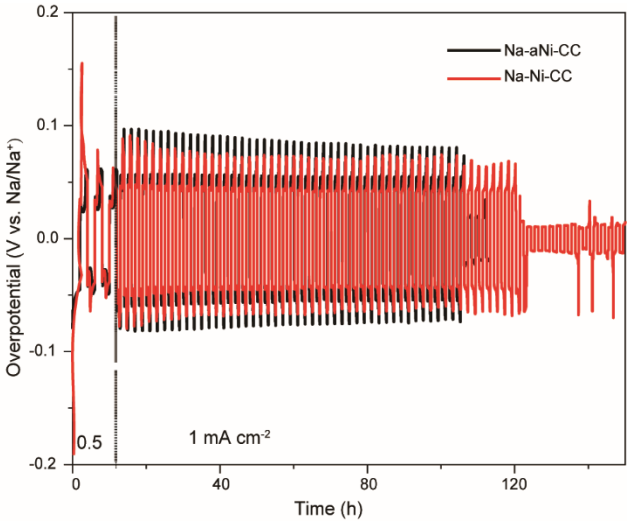

Figure S16. Stability of the symmetrical cell with Na-Ni-CC and Na-aNi-CC.

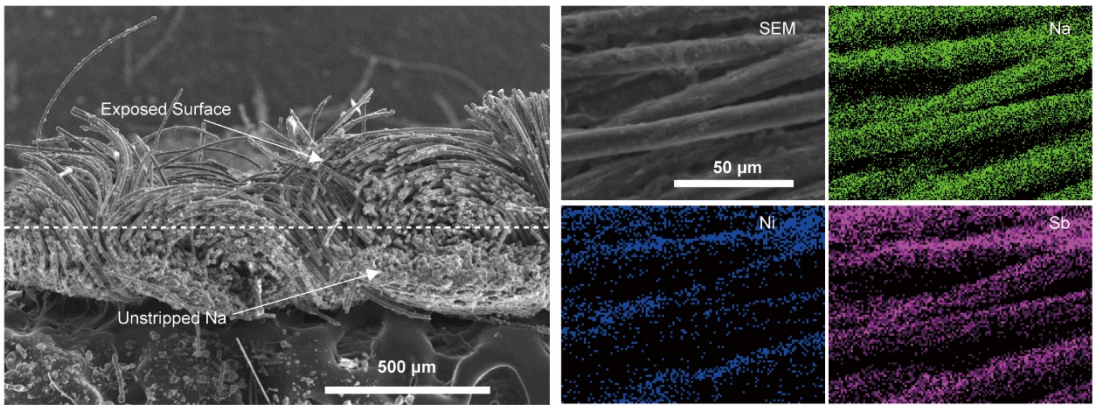

Figure S17. The morphology and EDS mapping of the Na-NiSb-CC after stripping for 7 mAh cm^{-2}. The surface of the fibers in Na-NiSb-CC was totally exposed after the stripping and could work as self-regulating interface in the following cycling.

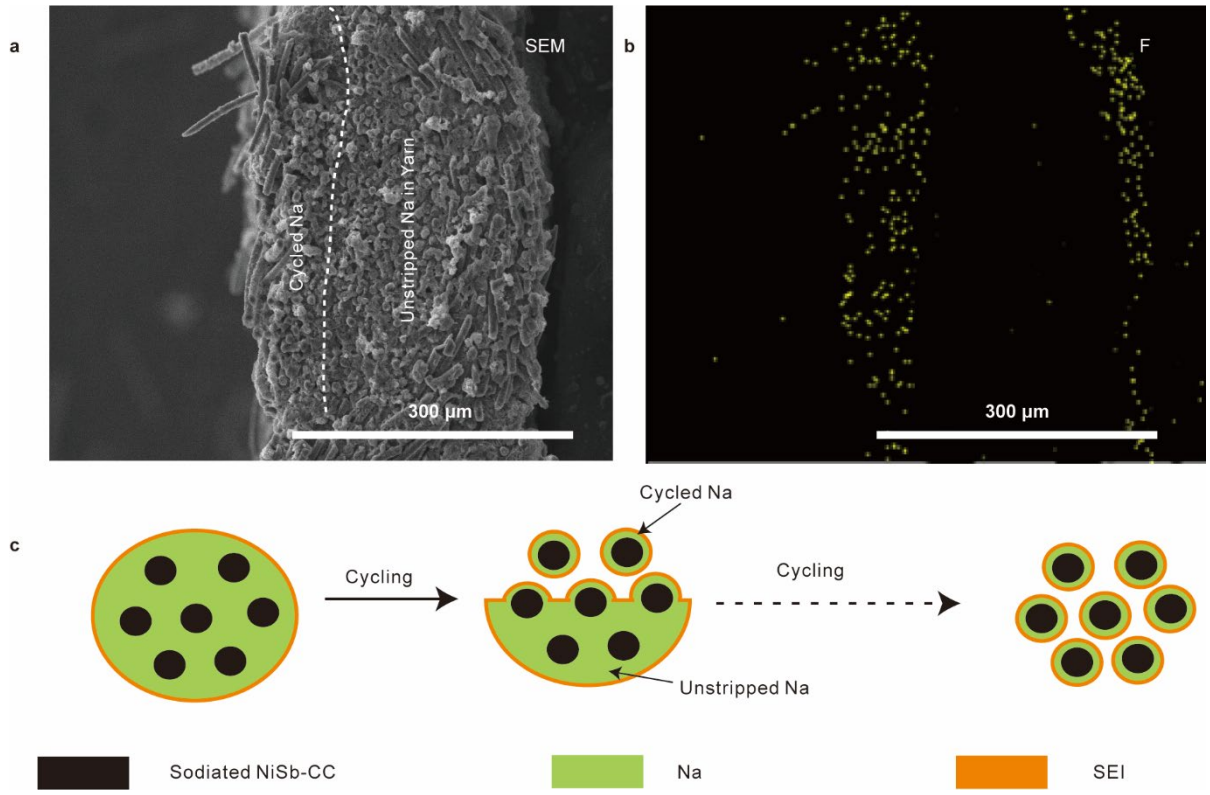

Figure S18. The SEI evolution in Na-NiSb-CC during cycling: a) the SEM image of the Na-NiSb-CC after cycling for 50th cycle at the capacity of 1 mAh cm^{-2}. The Na near the separator was stripped out and deposited back to the surface of the fibers in sodiated NiSb-CC. b) The EDS mapping of the F in a. The F element came from the NaF in SEI. c) the proposed model of evolution of SEI in Na-NiSb-CC.

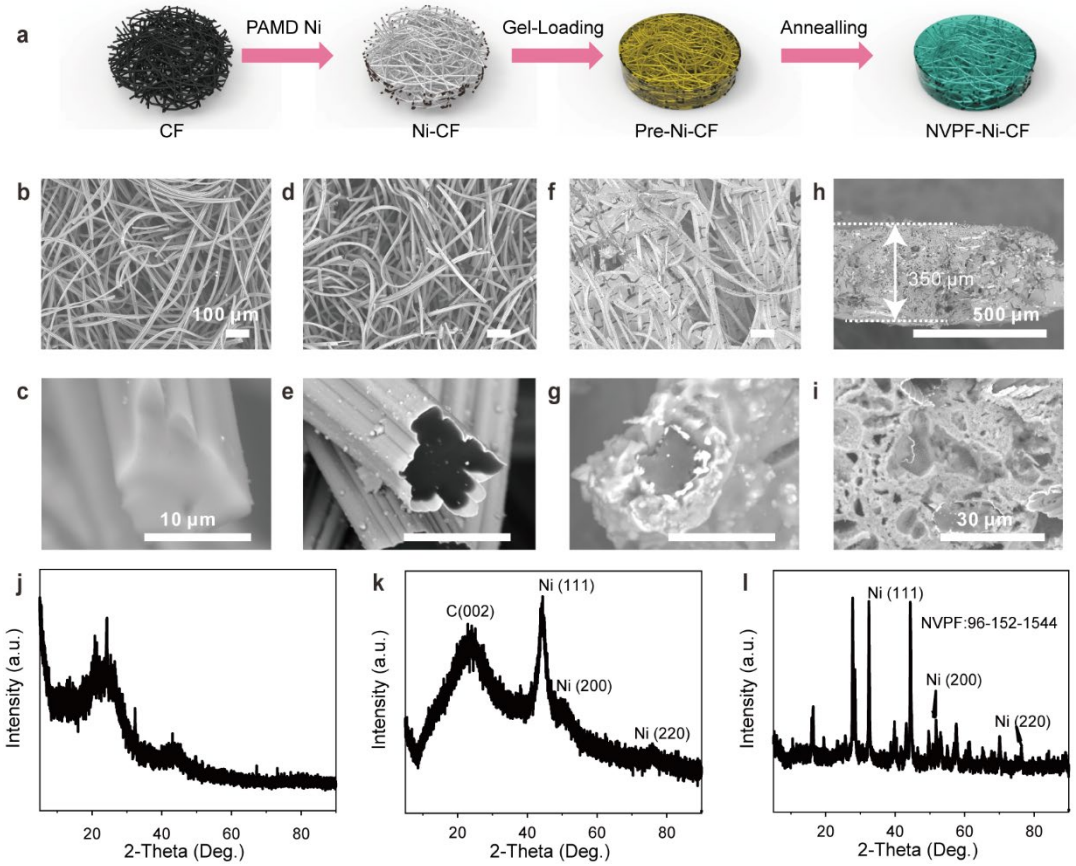

Figure S19. Preparation and characterization of binder-free cathode. a) Schematic illustration of the preparation process of ultra-thick sodium-vanadium fluorophosphate (NVPF) cathode. The item "Pre-Ni-CF" in the figure stands for the composited with precursor loaded in the host. b) SEM image of the carbon felt (CF). c) SEM image of a single fiber in the CF. d) SEM image of the Ni-coated CF (Ni-CF). e) SEM images of a single fiber in the Ni-CF, demonstrating the core-shell structure. f) SEM image of the binder-free Ni-CF supported NVPF cathode (NVPF-Ni-CF). g) SEM image of a single fiber in the NVPF-Ni-CF, demonstrating the success of the loading of active materials on the Ni-CF. h) Cross-sectional SEM image of the ultra-thick NVPF cathode with the mass loading of 55 mg cm^{-2}. i) Enlarged SEM image of h, demonstrating that each fiber inside the composite is coated with the NVPF active materials. j) XRD spectrum of the pristine CF. Two broad peaks at ~26° and ~42° correspond to the graphite-2H. k) XRD spectrum for the Ni-CF. New peaks arising at 44.5°, 52.8°, and 76.3° can be ascribed to the (002), (200), and (220) plane of the Cubic Ni. l) XRD patterns of the NVPF-Ni-CF cathode. Other peaks except for the Ni and CC can be attributed to NVPF.

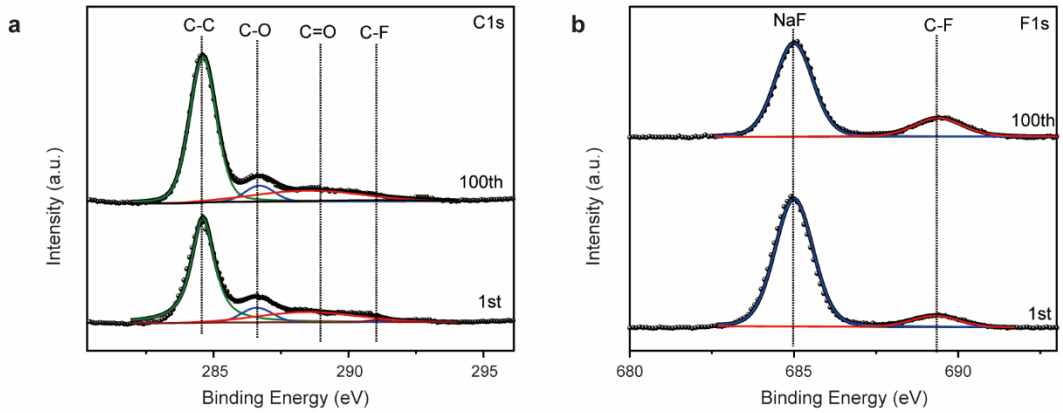

Figure S20. The XPS spectrums of Na-NiSb-CC after 1st cycle and 100th cycle, demonstrating that the SEI was robust and the constituents of SEI was not changed. a) The fine spectrum for C1s: The peak at 284.6 eV could be ascribed to the C-C bonds. The peak at 286 eV could be ascribed to the C-O. The peak at 289 eV could be attributed to C=O. The C-O and C=O may come from the organic content in the SEI. b) The fine XPS spectrum for F1s. The peak at 685 eV could be ascribed to the metal fluorides (NaF) in the SEI and peak at the 689 eV could be attributed to the organic fluorine (C-F).

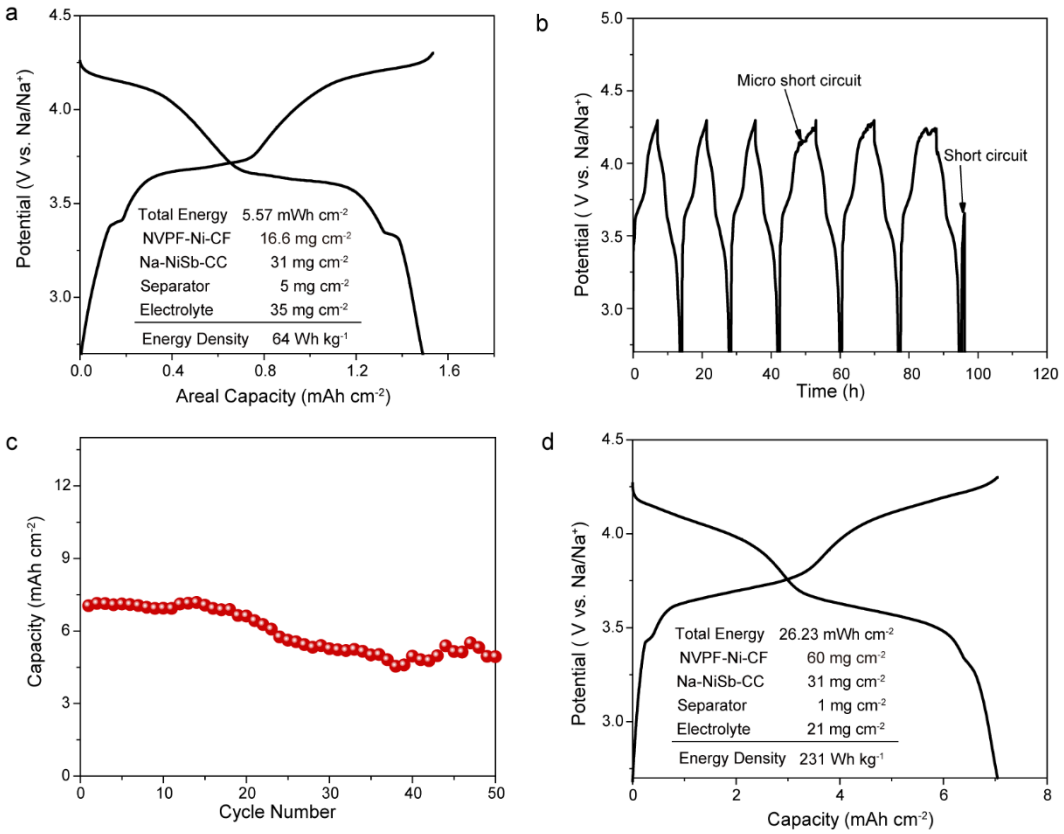

Figure S21. Electrochemical Performance of NVPF-Ni-CF||Na-NiSb-CC and NVPF-Ni-CF||Na-CC battery. a) GCD profiles for the NVPF-Ni-CF||Na-NiSb-CC with the low loading of the NVPF. The NVPF-Ni-CF||Na-NiSb-CC cell with a designed capacity of 1.49 mAh cm^{-2} delivers a limited energy density of 64 Wh kg^{-1}. b) Galvanostatic discharge-charge (GCD) profiles of the NVPF-Ni-CF||Na-CC with the areal capacity of 7 mAh cm^{-2}. The cell can only run for 3 cycles. c) Cycling stability for NVPF-Ni-CF||Na-NiSb-CC cell with Celgard separator and high areal capacity of 7 mAh cm^{-2} under the lean electrolyte condition (3 mg mAh^{-1}). d) GCD profiles of cell in c. The estimated energy density of the cell is higher than 230 Wh kg^{-1}.

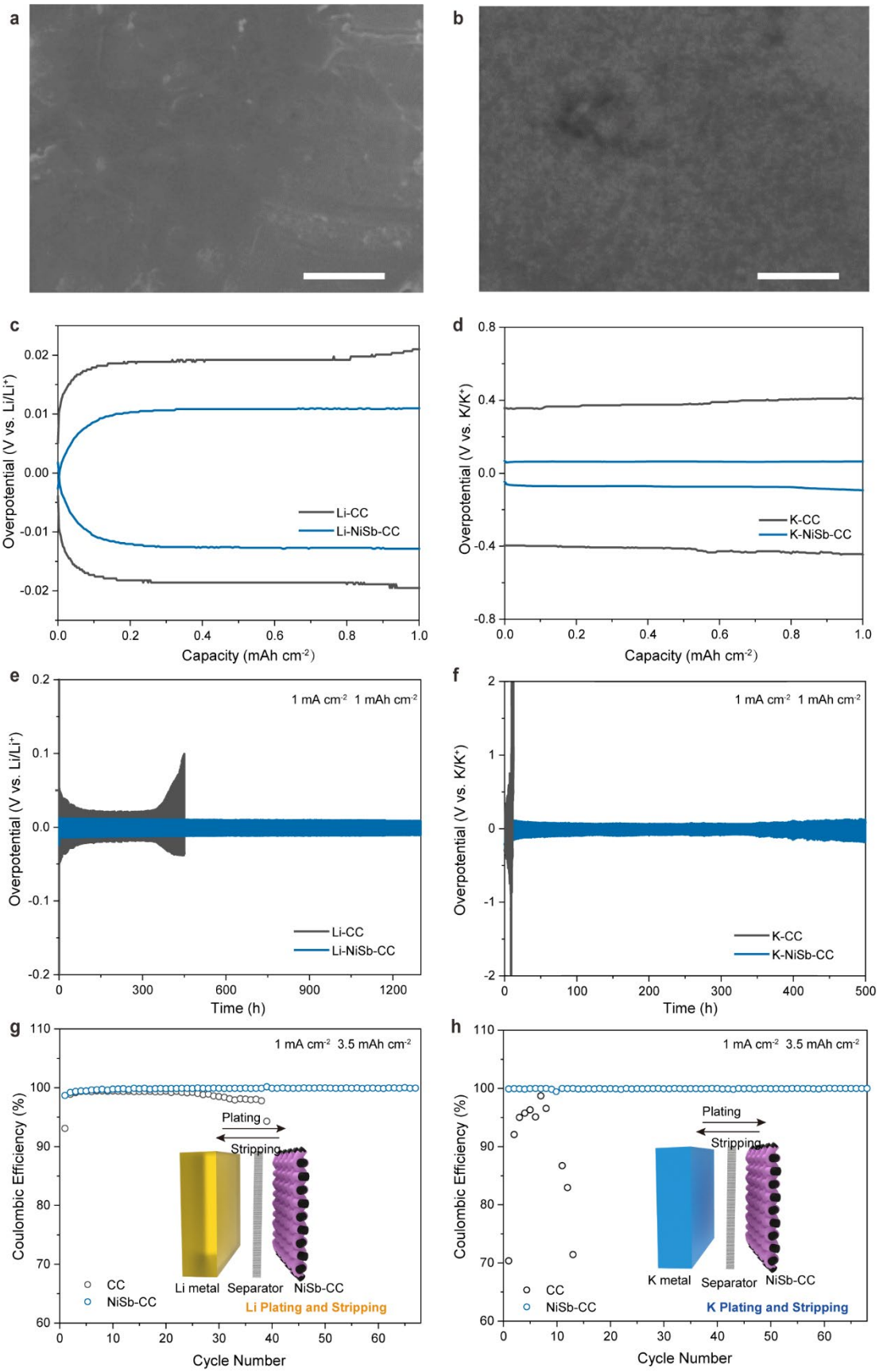

Figure S22. Versatility of the self-regulating mechanism to other metal anodes. a) Morphology of the NiSb coated Ni with the deposition of Li at the capacity of 0.75 mAh cm^{-2}. The scale bar in the figure represents 20 µm. b) Morphology of the NiSb coated Ni with the deposition of K at the capacity of 0.75 mAh cm^{-2}. The scale bar in the figure represents 20 µm. c) GCD profiles

of the symmetrical cells composed of different lithium anodes. d) GCD profiles of the symmetrical cells composed of different K anodes. e) Comparison of the durability of symmetrical cells with Li metal anodes based on different hosts cycling at the capacity of 1 mAh cm^{-2}. f) Comparison of the durability of symmetrical cells with K metal anodes based on different hosts cycling at the capacity of 1 mAh cm^{-2}. g) Evaluation of the Coulombic efficiencies for the plating and stripping of lithium on different current collectors. The insert in the figure is the typical structure of cells composed of lithium metal foil and current collectors. The arrows in the figure indicate the diffusions of lithium ions during the plating and stripping process. h) Evaluation of the Coulombic efficiencies for the plating and stripping of potassium on different current collectors. The arrows in the figure indicate the diffusions of potassium ions during the plating and stripping process.

Table S1. Comparation of the energy density of state-of-the-art SMBs.

Sample	Cathodic active materials (mg cm^{-2})	Cell mass* (mg cm^{-2})	N/P ratio	Areal capacity (mAh cm^{-2})	Energy density (Wh kg^{-1})	Ref.
NVP||Na/SbF_3	1.0	30.79	255	0.09	9.79	[6]
NVP||Na/$SnCl_2$	1.5	38.41	153	0.15	13.27	[7]
NVP||Na/C@Sb	2.0	28.34	33	0.18	21.59	[8]
NVP||NG-NF@Na	1.5	43.16	36	0.14	10.94	[9]
NNM||Na-C	10.0	188.58	143	0.82	1.42	[10]
O_2||Na/NSCNT**	1.0	28.69	46	0.5	34.8	[11]
NMHCF||Na	3.0	34.19	64	0.36	37.29	[12]
CC@0.5MnO_2@ Na_2S_6||Na	1.7	38.89	23	1.02	41.35	[13]
$NaVOPO_4$/C||Na	2.0	32.04	79.3	0.29	31.46	[14]
ZCS@S||Na	5.0	35.44	10.7	2.15	54.17	[15]
NVPF-NiCF|| Na-NiSb-CC	**12**	**87.6**	**14.1**	**1.49**	**63.58**	**This Work**
NVPF-NiCF|| Na-NiSb-CC	**56.0**	**131**	**3**	**7.02**	**200.76**	
NVPF-NiCF|| Na-NiSb-CC	**56.0**	**113**	**3**	**7.02**	**231.23**	

*Assuming the sodium metal plate processes the thickness of 200 um and the mass of sodium is 20 mg cm^{-2}, equaling to an areal capacity of 23 mAh cm^{-2}. The areal mass of the separator GF/C and GF/D provided by Whatman were 5.19 mg cm^{-2} and 12.54 mg. Total mass included the cathode, anode, and separator. The thickness of the Al foil was 15 μm, and the mass is 4 mg cm^{-2}; The areal mass of the Cu foil used in the lab is 9 mg cm^{-2}. The areal mass of the carbon cloth was 12 mg cm^{-2}. The mass of Ni foam with an area of 1cm^2 weighed 28 mg. The mass of the electrode included the current collector, binders, conductive agents, and the active materials. The mass of the electrolyte was not included in the reported batteries as the amount was not mentioned.

**For the oxygen-based battery, the mass of active materials in the cathode was calculated based on the quantity of the catalyst.

References

[1] J. Xia, F. Chen, J. Li, N. Tao, *Nat. Nanotechnol.* **2009**, *4*, 505.

[2] J. R. Miller, R. A. Outlaw, B. C. Holloway, *Science* **2010**, *329*, 1637.

[3] Q. Pan, Y. Wu, W. Zhong, F. Zheng, Y. Li, Y. Liu, J. Hu, C. Yang, *Energy Environ. Mater.* **2020**, *3*, 186.

[4] Q. Pan, Y. Wu, F. Zheng, X. Ou, C. Yang, X. Xiong, M. Liu, *Chem. Eng. J.* **2018**, *348*, 653.

[5] S. H. Dong, C. X. Li, L. W. Yin, *Eur. J. Inorg. Chem.* ***2018****, 2018, 992.*

[6] Z. Xu, J. Yang, T. Zhang, L. Sun, Y. Nuli, J. Wang, S.-i. Hirano, *Adv. Funct. Mater.* **2019**, *29*, 1901924.

[7] X. Zheng, H. Fu, C. Hu, H. Xu, Y. Huang, J. Wen, H. Sun, W. Luo, Y. Huang, *J. Phys. Chem. Lett.* **2019**, *10*, 707.

[8] G. Wang, Y. Zhang, B. Guo, L. Tang, G. Xu, Y. Zhang, M. Wu, H.-K. Liu, S.-X. Dou, C. Wu, *Nano Lett.* **2020**, *20*, 4464.

[9] C. Bao, B. Wang, Y. Xie, R. Song, Y. Jiang, Y. Ning, F. Wang, T. Ruan, D. Wang, Y. Zhou, *ACS Sustainable Chem. Eng.* **2020**, *8*, 5452.

[10] S.-S. Chi, X.-G. Qi, Y.-S. Hu, L.-Z. Fan, *Adv. Energy Mater.* **2018**, *8*, 1702764.

[11] B. Sun, P. Li, J. Zhang, D. Wang, P. Munroe, C. Wang, P. H. L. Notten, G. Wang, *Adv. Mater.* **2018**, *30*, 1801334.

[12] H. Gao, S. Xin, L. Xue, J. B. Goodenough, *Chem* **2018**, *4*, 833.

[13] A. Kumar, A. Ghosh, A. Roy, M. R. Panda, M. Forsyth, D. R. MacFarlane, S. Mitra, *Energy Storage Mater.* **2019**, *20*, 196.

[14] Y. Fang, Q. Liu, L. Xiao, Y. Rong, Y. Liu, Z. Chen, X. Ai, Y. Cao, H. Yang, J. Xie, C. Sun, X. Zhang, B. Aoun, X. Xing, X. Xiao, Y. Ren, *Chem* **2018**, *4*, 1167.

[15] H. Liu, W. Pei, W.-H. Lai, Z. Yan, H. Yang, Y. Lei, Y.-X. Wang, Q. Gu, S. Zhou, S. Chou, H. K. Liu, S. X. Dou, *ACS Nano* **2020**, *14*, 7259.